3rd YEAR INTERNSHIP REPORT

General engineering degree
Physics and Modelling Department
2018-2019

QUALIFICATION OF THE BCM1F DETECTOR FOR LUMINOSITY MEASUREMENT IN THE CMS EXPERIMENT

Younes OTARID
Class 2019

Supervisor :
Georg Auzinger - georg.auzinger@cern.ch

CERN
Route de Meyrin, 1211 Genève

1st March 2019 - 31st August 2019

Abstract

Qualification of the BCM1F Detector for Luminosity Measurement in the CMS Experiment

At the European Organisation for Nuclear Research (CERN), experiments aim at producing and studying rare physical interactions that result from particle collisions using the Large Hadron Collider (LHC). The key parameters to evaluate the performance of particle colliders for this purpose are the luminosity and the beam energy. The Luminosity is the characteristic quantity that provides a measure of the ability of a collider to produce a certain number of specific particle interactions. It is also important as it is used as normalisation in cross-section measurements performed in the scope of physics analysis. Therefore, high accuracy of the luminosity measurements is essential for the accelerator operation and for the analysis of the physics data.

At the Compact Muon Solenoid (CMS) experiment, several detectors measuring luminosity are deployed under the responsibility of the Beam Radiation Instrumentation Luminosity (BRIL) group. One of these luminometers is the Fast Beam Conditions Monitor (BCM1F). The Run2 version of the detector was composed of a combination of Polycrystalline Diamond sensors (pCVD) and Silicon sensors (Si). However, during operations, silicon sensors showed better performance with respect to the diamond sensors that suffered from efficiency loss. As Long Shutdown 2 (LS2) of the LHC is going on, the BCM1F detector that suffers from radiation damage will be replaced by a newly built version based entirely on AC-coupled silicon sensors. C-shape modules and test-boards were produced and mounted with the new AC-coupled silicon sensors. Thus the need of a test beam campaign and a full characterization in order to study the performance of the new sensor design.

The first chapter introduces the reader to the LHC and the CMS experiment, as well as LHC specific terminology and quantities. Chapter 2 presents the concept of Luminosity and its measurement within the CMS Experiment. Chapter 3 summarizes basic concepts of Silicon based detectors. A description of the BCM1F detector and the BCM1F signal chain is then provided in Chapter 4. Chapter 5 and 6 provide information about the DESY test-beam facility, the tested prototype and the data acquisition software framework. The BCM1F DAQ system integration is also discussed and implementations of dedicated tools are presented. Finally, in Chapter 7, sensor characterisation results are presented. A conclusion is drawn in Chapter 8 where a summary of the testbeam campaign and the analysis prospects are provided.

Résumé

Caractérisation du Détecteur BCM1F pour la Mesure de Luminosité dans l'Expérience CMS

Au Centre Européen de la Recherche Nucléaire (CERN), les expériences ont pour objectif de produire et d'étudier des phénomènes physiques rares résultant de la collision de particules au moyen du Grand Collisionneur à Hadrons (LHC) . Les paramètres clés pour l'évaluation des performances des collisionneurs à cet égard sont la Luminosité et l'énergie du faisceau. La Luminosité est la quantité décrivant la capacité d'un collisionneur à produire un certain nombre d'interactions spécifiques de particules. Elle est également importante dans la mesure où celle-ci est utilisée dans la normalisation des mesures de sections efficaces effectuées dans le cadre des analyses de physique. Une grande précision dans la mesure de Luminosité est dès-lors essentielle au fonctionnement des collisionneurs ainsi qu'aux analyses de données de physiques.

Dans l'expérience CMS, plusieurs détecteurs en charge de la mesure de luminosité sont déployés sous la responsabilité du groupe BRIL. L'un de ces luminomètres est le Fast Beam Conditions Monitor (BCM1F). La version incluse lors du Run2 est basée sur une combinaison de capteurs Diamant PolyCrystallin (pCVD) et de capteurs Silicium (Si). Cependant, lors du Run2, les capteurs Sillicium ont démontré des performances supérieures à celles des capteurs Diamant qui se sont avéré souffrir d'une perte d'efficacité. L'arrêt Long Shutdown 2 (LS2) étant en cours, le détecteur BCM1F endommagé par les fortes doses de radiations, sera remplacé par une nouvelle version entièrement basée sur des capteurs Silicium AC-couplés. Des modules C-shape et des modules de test ont été produits et équipés des nouveaux capteurs Sillicium AC-couplés. D'où le besoin d'une campagne de test en faisceaux et d'une caractérisation intégrale des capteurs afin d'étudier les performances du nouveau design.

Le premier chapitre introduit le lecteur au Large Hadron Collider et à l'expérience Compact Muon Solenoid, ainsi qu'à la terminologie et aux quantités spécifiques au LHC. Le Chapitre 2 présente le concept de Luminosité ainsi que sa mesure au sein de l'expérience CMS. Le Chapitre 3 résume quelques concepts de base des détecteurs à Silicium. Une description du détecteur BCM1F ainsi que de sa chaine de signal est proposée au Chapitre 4. Le Chapitre 5 et 6 présente l'infrastructure de test en faisceaux à DESY, le module testé ainsi que l'environnement informatique d'acquisition de données. L'intégration des systèmes d'acquisition de données du détecteur BCM1F, ainsi que l'implémentation des outils nécessaires sont également présentés. Enfin, au Chapitre 7, les résultats de la caractérisation des capteurs Silicium sont présentés. Une conclusion est proposée dans le Chapitre 7 où un résumé de la campagne de test en faisceaux ainsi qu'une vue des analyses avenir sont fournis.

Acknowledgements

I would first like to profoundly thank Anne Dabrowski, David Barney and Georg Auzinger for offering me the opportunity to work under their guidance and in such a great environment. It has been a real honour to be part of the BRIL project.

Very special thanks to my supervisor Georg Auzinger for all the invaluable help and guidance he has given me through these six months. I want to thank him deeply for his trust, his dedication and his encouragements. I greatly learned from his knowledge and his experience. By his side, I have been given not only his patience and support, but also the autonomy for which I am highly grateful. So many thanks to you Georg.

Secondly I would like to thank Alexander Ruede, Moritz Guthoff and Ziheng Chen for their precious help and contribution to my work. The performed studies and the various developments have greatly profited from their invaluable experience.

Finally, I would like to thank the whole BCM1F team for considering my work and for being actively involved in the discussions related to it. They all have been of great support in the working process.

Table of contents

List of figures

Abbreviations

AC Alternating Current

ADC Analog-to-Digital Converter

AMC Advanced Mezzanine Card

AOH Analog Opto-Hybrid

ASIC Application Specific Integrated Circuit

BCM1F Fast Beam Conditions Monitor

BRIL Beam Radiation Instrumentation and Luminosity

CCE Charge Collection Efficiency

CERN European Council for Nuclear Research

CMS Compact Muon Solenoid

DAQ Data Acquisition

DC Direct Current

DESY Deutsches Elektronen-Synchrotron

DOH Digital Opto-Hybrid

FMC FPGA Mezzanine Card

FPGA Field Programmable Gate Array

FWHM Full Width Half Maximum

GLIB Gigabit Link Interface Board

I2C Inter-Integrated Circuit

IPMI Intelligent Platform Management Interface

IP Interaction Point

LED Light Emitting Diode

LHC Large Hadron Collider

LLD Linear Laser Driver

LVDS Low Voltage Differential Signaling

MCH MicroTCA Control Hub

MIB Machine Induced Background

MIP Minimum Ionizing Particle

NIM Nuclear Instrumentation Module

PAM Pulse Amplitude Modulation

PCB Printed Circuit Board

pCVD Polycrystalline Diamond Sensors

PLL Phase Locked Loop

PMT Photo-Multiplier Tube

TLU Trigger Logic Unit

TTL Transistor-Transistor Logic

1 Introduction

1.1 European Organization for Nuclear Research (CERN)

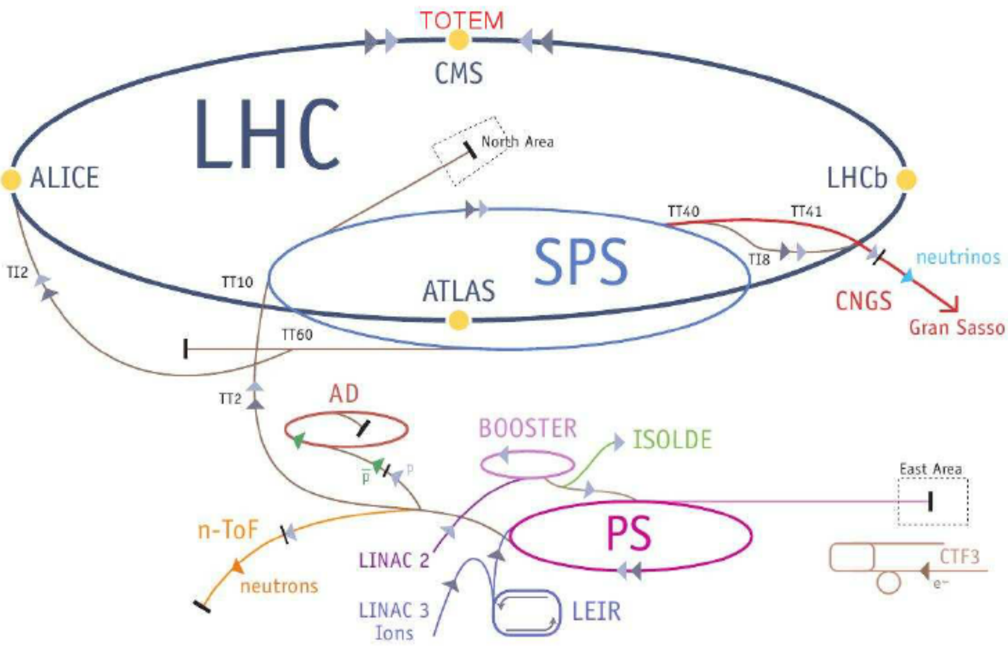

Figure 1.1 – LHC injection and acceleration chain at CERN [1]

Founded in 1954, the European Laboratory for Nuclear Research (CERN) sits astride the Franco-Swiss border near Geneva. It was one of Europe's first joint ventures and now has 22 member states. At CERN, more than 10000 physicists and engineers from 100 countries around the world are probing the fundamental structure of the universe. They use the largest and most complex scientific instruments to reveal the building blocks of matter - the fundamental particles [1].

The Large Hadron Collider is the largest scientific instrument ever built by mankind and at the same time the most powerful particle accelerator in the world. It was constructed in an underground tunnel with a circumference of 27 kilometers that was initially excavated for the LHC's predecessor, the Large Electron Positron Collider, beneath the French-Swiss border in the Geneva region. It is capable of colliding two proton beams at a center of mass energy of 14 TeV. This collision energy is achieved by accelerating the bunched proton beams through several stages before the injection phase into the LHC accelerator ring. The different stages and accelerators are presented in Figure 1.1.

The Standard Model of Particle Physics, that provides a consistent theoretical description of all elementary particles as well as the fundamental forces that govern their interactions, is studied in the four main experiments at the LHC. The ATLAS and CMS experiments are general-purpose detectors built to investigate a broad range of physics phenomena. As they were designed independently and use different observation approaches of the same phenomena, they allow cross-confirmation of new discoveries. The ALICE and LHCb experiments are dedicated to specific phenomena and have very specialized detector systems.

1.2 Compact Muon Solenoid Experiment (CMS)

The Compact Muon Solenoid (CMS) detector is made of several stages of sub-detectors to accurately track and study the products of the particle collisions that happen in the center of the detector. It consists of various concentric layers and integrates one of the most powerful solenoid magnets ever built, capable of producing a magnetic field of up to 4 Tesla [2]. The CMS detector is briefly described in Figure 1.2.

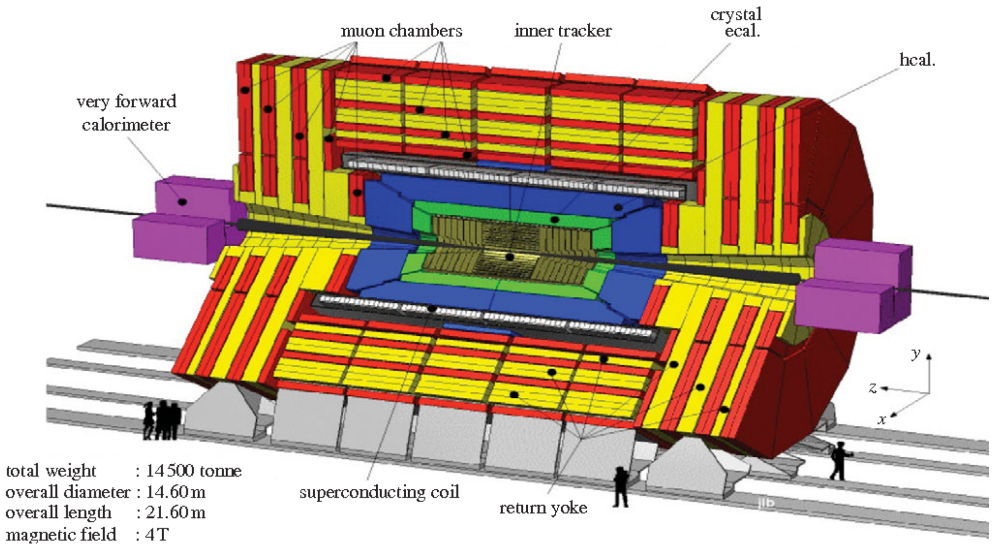

FIGURE 1.2 – Cutway view of the CMS detector [2]

In 2012, both the ATLAS collaboration and the CMS collaboration announced the discovery of the Higgs Boson, one of the most important discoveries in fundamental physics [3].

The LHC is colliding two proton beams accelerated in opposite direction, each made of several bunches of about 100 billion protons. Each bunch is circulating in the beam pipe with a revolution frequency of 11.245 kHz. The circulating bunches are arranged following the so called LHC filling scheme that describes a certain bunch pattern. Bunches are usally grouped in bunch trains where the bunches are spaced at 25ns. Both beams can contain up to 2808 bunches. At the center of each experiment or what is called the Interaction Point (IP), the bunches of the two circulating beams collide with the so called bunch frequency of 40.08 MHz.

In every bunch crossing there are potentially more than 60 so-called inelastic proton-proton collisions that lead to the desired scattering and the creation of collision products. The CMS subdetectors then track the trajectory of these products and measure their properties. The collected data is then stored and further processed. The main purpose is to have them studied and evaluated to potentially reveal new phenomena beyond the Standard Model.

2 Luminosity Measurement

2.1 The Concept of Luminosity

In particle physics experiments, besides the energy available for the production of new effects, the number of useful interactions (events) is an important parameter. The ability of a particle accelerator to produce a number of interactions is quantified by the so-called luminosity L which is the proportionality factor between the number of observed particle interactions (events) per time interval dR/dt, and the cross section σ_p that describes the probability of the occurence of a certain process produced by the interaction :

$$\frac{dR}{dt} = L \cdot \sigma_p \tag{2.1}$$

The luminosity mainly depends on the number of particles in the colliding bunches and the transverse beam size at the interaction point. Since physicists are mainly looking for processes with very low production cross section, they seek to increase the luminosity in order to reach higher event rates and thus better statistical information of that process. A constant feedback of luminosity measurements is therefore needed not only for accelerator performance monitoring and beam optimization, but also to determine the production cross-section of observed events.

2.2 The Zero-Counting Algorithm

Any detector able to measure particle hit rates in linear dependency of the luminosity can be used as a luminometer. The Zero-Counting Algorithm is a way to evaluate luminosity per bunch crossing using the measured hit rate [4]. It is only valid for detectors with low occupancy, or probability of a hit in a bunch crossing. As the number of hits per bunch crossing follows a Poissonian distribution, with probability p of a certain number of hits n :

$$p(n) = \frac{\mu^n e^{-\mu}}{n!} \tag{2.2}$$

By counting the number of bunch crossings without interaction (zero counting), when the probability of having two or more interactions per bunch crossing becomes non-negligible, the mean value of occuring hits μ, also called occupancy, can be determined. The probability of *zero* hits *p(0)* in that bunch crossing can be determined using the measured hit rate N_{hits}/N_{bc} in a particular bunch crossing [5] :

$$\mu = -ln[p(0)] = -ln[1 - p(n \neq 0)] = -ln[1 - \frac{N_{hits}}{N_{bc}}] \tag{2.3}$$

The per-bunch luminosity L_{bunch} can then be calculated using the μ of that bunch crossing, the detector-dependent visible cross-section σ_{vis} and the collider revolution frequency f, as :

$$L_{bunch} = \frac{\mu}{\sigma_{vis}} \cdot f \tag{2.4}$$

The visible cross-section is a detector-depedent quantity and refers to all the cross sections of the processes that are observable by the detector. Calibrating the luminometer and determining the visible cross-section is achieved in the so-called Van-der-Meer scan [6]. In this method, special experimental conditions are created, where the two beams are scanned against each other with gradually increasing displacement. By measuring the hit rate as a function of the beam displacement in two planes, it is possible to calculate the visible cross-section.

2.3 BRIL Project and Luminosity Measurement at CMS

The luminosity measurement at CMS is done online and offline. Results provided by online bunch by bunch luminosity measurement are provided to the experiment and the accelerator control rooms every 1.457s. Various sub-detectors for luminosity measurements are designed and operated independentally under the responsability of the Beam Radiation Instrumentation and Luminosity (BRIL) project. Some of the BRIL sub-detectors are shown in Figure 2.1.

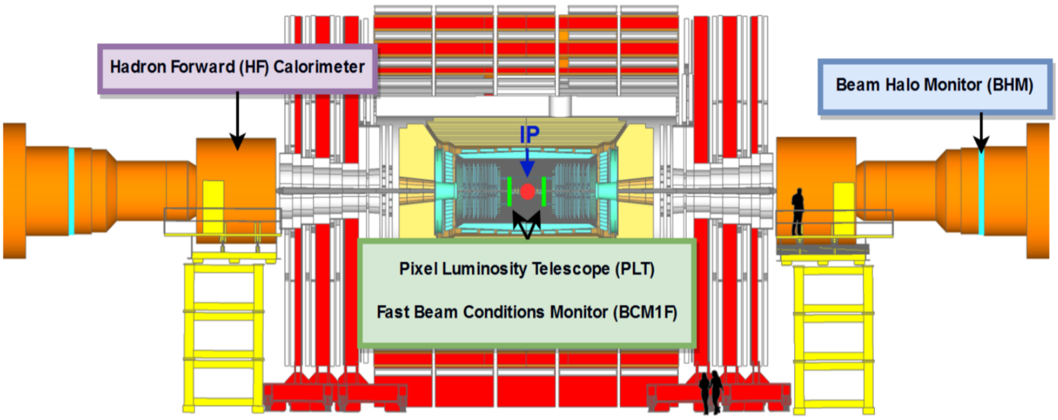

FIGURE 2.1 – Overview of some of the BRIL sub-detectors [7]

The Pixel Luminosity Telescope (PLT) is an online luminometer that has some similarities with the CMS pixel tracker when it comes to sensors and readout electronics. The Fast Beam Conditions Monitor (BCM1F) is built for luminosity measurements as well as Machine Induced Background (MIB) measurement created by the beam or beam halo interaction with residual gas in the vacum chambers. The Hadron Forward (HF) Calorimeter is also used in luminosity measurement but with a different read out design.
Each sub-detector is operated independently, allowing for continuous cross check and tracking of possible detector malfunctions.

3 Physics of Silicon Detectors

3.1 Silicon as a Semiconductor and the PN-Junction

Ultra-pure Silicon is an industrially produced material in the form of a regular crystal that shows typical properties of a semiconductor : It acts as an insulator at low temperatures, and shows conductance at higher temperatures. This behavior is explained by the quantum-mechanical properties given the configuration of the silicon atoms within the regular lattice of the crystal. Silicon is a group-IV element and has four valence electrons that can be excited to a free state by adding energy exceeding a threshold that is characteristic to the material. In intrinsic silicon (non-doped silicon) this band gap separating the valence band and the conduction band is 1.12 eV. However, the conductivity behavior of silicon can be changed by adding additional states within this band gap. These additional levels facilitate transitions from one band to the other. This process is called doping. Dopants are tipically group-V or group-III elements and act as sources of additional charge carriers or as traps, creating 'n-type and 'p-type' silicon.

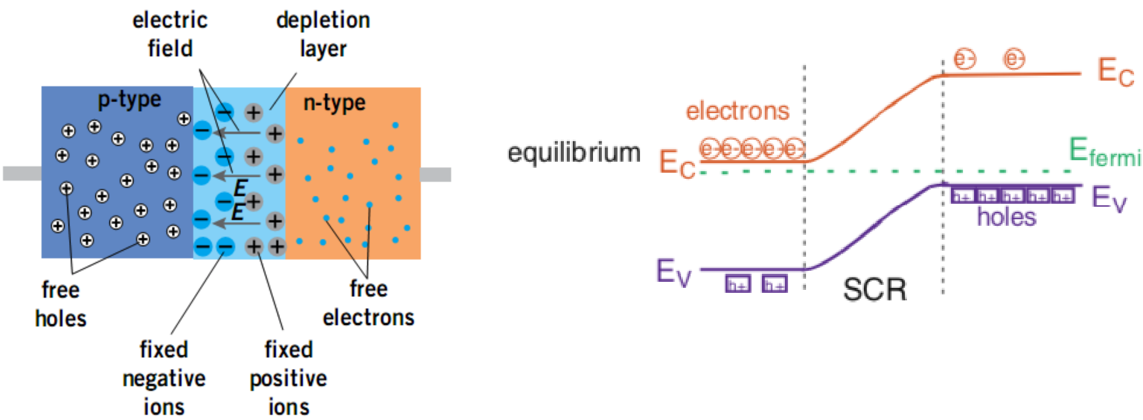

FIGURE 3.1 – PN-junction sketch (left) and band diagram (right) [8]

In intrinsic silicon, thermal excitation is constantly creating electron-hole pairs, which does not make it appealing for a particle detector as the number of charge carriers created by a traversing particle through ionization is rather small compared to the intrinsic density. To obtain a measurable signal, silicon needs to be depleted of free carriers. This is done by applying a reverse bias voltage to a p-and n-type silicon brought into contact, or so-called *pn-junction* shown in Figure 3.1. In this junction, in thermal equilibrium, the alignment of the two Fermi-energy levels moves the valence and conduction bands, thus creating the space-charge region through the electrical field induced by the diffusion and recombination currents between the two differently-doped regions [9]. This space-charge region is then depleted of free carriers and can be exploited to produce signals created by charged particles traversing the silicon.

3.2 Energy Loss - Signal Creation

Ionizaton is the principle by which particles are detected in their interaction with matter. In silicon detectors, traversing particles create electron-hole pairs when losing energy. A quantification of this energy loss is realised in the Bethe-Bloch formula [10] :

$$-\frac{dE}{dx} = 4\pi\rho N_A r_e^2 m_c c^2 z^2 \frac{Z}{A}\frac{1}{\beta^2}[\frac{1}{2}ln(\frac{2m_e c^2\beta^2\gamma^2 T_{max}}{I^2}) - \beta^2 - \frac{\delta(\gamma)}{2}] \tag{3.1}$$

where z is the charge of the incident particle, T_{max} the maximum kinetic energy that can be transfered to a single electron in collision, I the mean excitation energy, Z the atomic number, A the atomic mass, N_A the Avogadro number. m_e the electron mass, c the speed of light, r_e the classical electron radius, β the reletivistic beta v/c, $\gamma = 1/\sqrt{1-\beta^2}$ and δ a density effect correction.

Figure 3.2 shows the differential energy loss of muons in iron as a function of incident momentum. The minimum around 500 MeV represents the minimum deposited energy in the material and muons of that energy are called Minimum-Ionizing Particles (MIPs). As these MIPs are hard to detect, they usually serve as benchmarks for detectors. The deposited charge in a thin layer follows a so-called Landau distribution that takes into consideration statistical fluctuations related to the energy loss. The probability-density function reads [11] :

$$p(x;\mu,c) = \frac{1}{\pi c}\int_0^\infty e^{-t} cos(t(\frac{x-\mu}{c}) + \frac{2t}{\pi}log(\frac{t}{c}))dt \tag{3.2}$$

with μ being the most probable value, and c being the scale parameter. An example of such a Landau distribution is given in Figure 3.2.

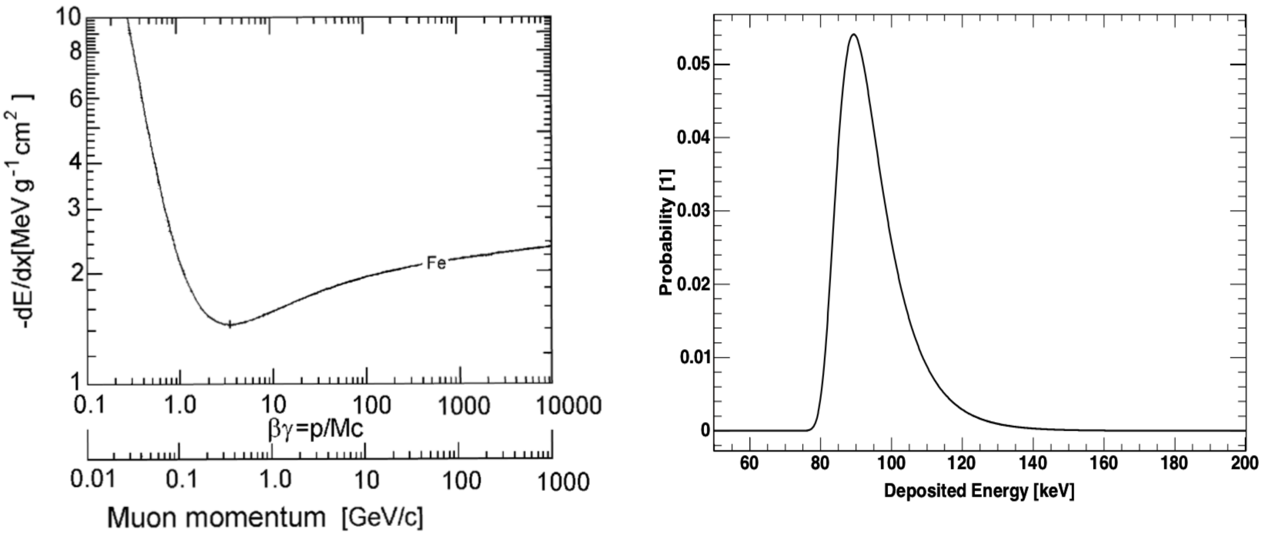

Figure 3.2 – Differential energy loss of muons in iron for different incident particle energies calculated with the Bethe-Bloch formula (left) [12], and the Landau distribution (right)

In order to create an electron-hole pair in silicon material, a particle has to deposit an energy of 3.6 eV, which is three times higher than the band gap energy. The most probable number of electron-hole pairs that are created in silicon per μm is $\sim$ 78, which yields about 22,000 electron-hole pairs in a 300 μm-thick sensor. As these electrons and holes drift inside the electrical field inside the detector bulk, a current is induced in the electrodes and a signal can be detected using specific read out electronics.

4 The BCM1F detector

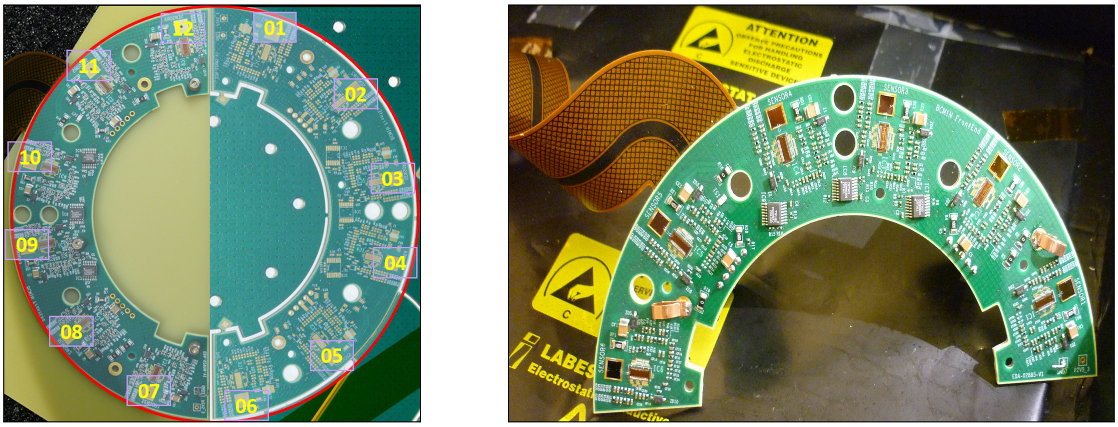

FIGURE 4.1 – Picture of one BCM1F C-Shaped module (right) and two joined BCM1F C-shapes (left) [5]

4.1 System Design

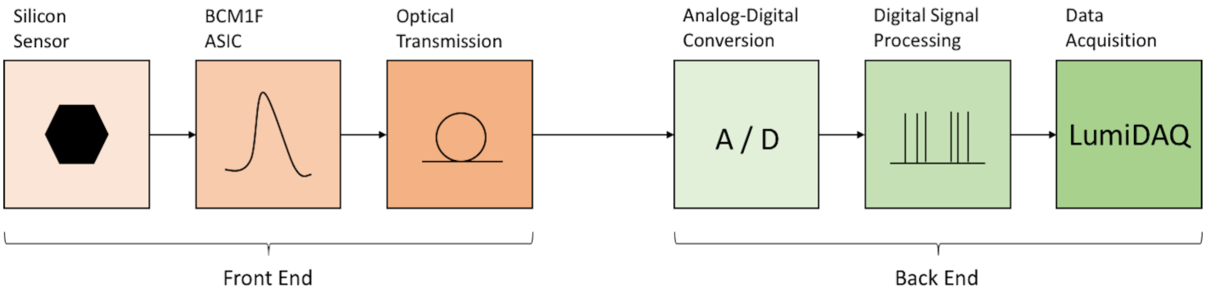

FIGURE 4.2 – BCM1F MicroTCA architecture block diagram

The BCM1F detector is an online luminometer installed within the CMS detector, around the beam pipe, at 1.83m from the interaction point (IP), that provides luminosity and machine induced background measurements to the CMS experiment. It consists of a C-shaped PCB, as shown in Figure 4.1, with 24 diamond and silicon sensors along with dedicated front end readout Application-Specific Integrated Circuits (ASICs) that shape and amplify the sensor signal. These signals are transmitted via an optoelectronic transmission chain to a custom back end electronics system. Signals are sampled, digitized and further processed by a Field-Programmable Gate Array (FPGA) and read out by the BRIL data acquisition software. The BCM1F back end electronics system includes two independent systems, the Versa Module Eurocard (VME) system and the newer Micro Telecommunication Computing Architecture (MicroTCA) system. A block diagram of the BCM1F MicroTCA architecture is depicted in Figure 4.2.

4.2 Front-End System

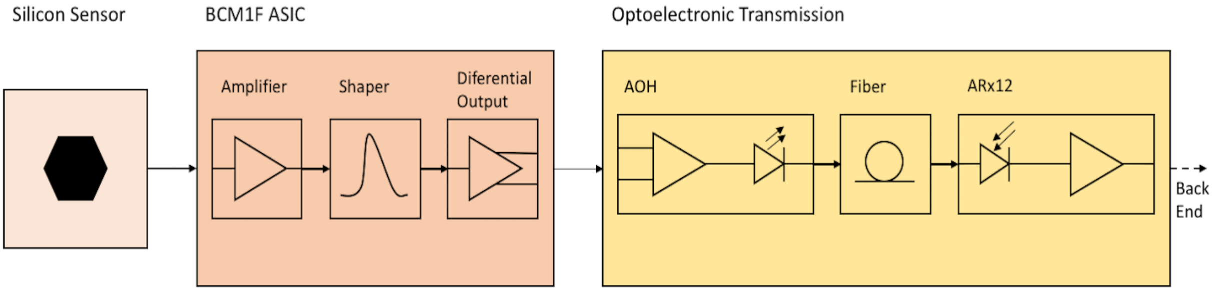

FIGURE 4.3 – BCM1F Front-End Block Diagram

The BCM1F front end electronics consists of the sensors, read out ASICs and the optoelectronic transmission path. The sensors and ASICs are mounted on two C-shaped parallel flex-rigid PCBs held by carbon fiber carriages perpendicular to the beam pipe. These C-Shapes are positioned in such a way that they encircle the beam pipe and thus place sensors radially at 7.2cm around the beam pipe and at a distance of $\pm 1.83m$ from the interaction point (IP). A block diagram of the front end electronics system is shown in Figure 4.3.

4.2.1 Sensors

In the Run2 version of the BCM1F detector, Silicon and Diamond sensors were used. Diamond was included as it provides many advantages over Silicon (radiation hardness, bigger band gap, low dark current ...). However, during Run2, Silicon showed better performance than Diamond that had several problems with efficiency loss. The new versions of the BCM1F detector are fully equiped with AC-coupled double diode Silicon sensors. The latter provide an active area of $1.7 \times 1.7mm^2$ and are equiped with a $100\mu m$ width guard-ring that can be either grounded or kept floating. A picture and a sketch of the sensors are shown in Figure 4.4.

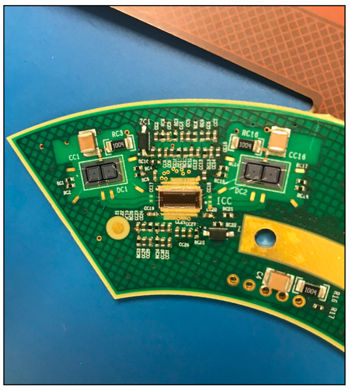

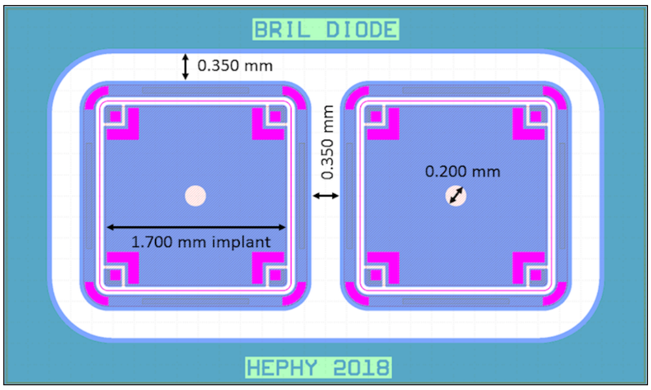

FIGURE 4.4 – Picture (left) and sketch (right) of the Silicon sensors

4.2.2 Front-End ASIC

The BCM1F ASIC is produced in the IBM 130nm CMOS RF process chosen for its radiation hardness. A fast transimpedance preamplifier with active feedback, a shaping stage and high-performance differential output buffer are integrated to the chip. Many other features are also provided such as the test pulse trigger that allows for ASIC functionality checks and detector calibration. A block diagram of single front end channel is shown in Figure 4.5.

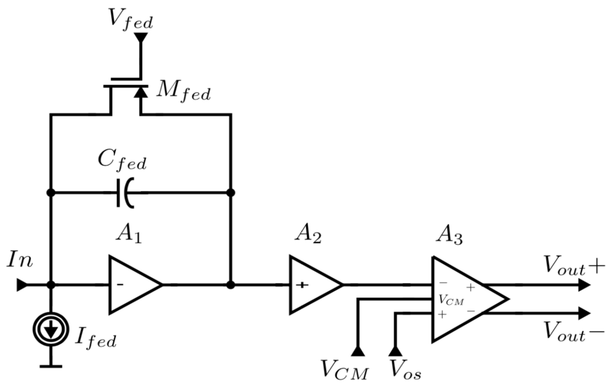

FIGURE 4.5 – Block diagram of a single BCM1F ASIC FE channel [13]

One channel consists of the transimpedance preamplifier with active feedback (A1), shaper stage (A2) and output buffer working as a single-ended–to–differential converter driving a 100 Ω external termination resistor (A3). The ASIC was designed to keep the full-width-half-maximum response below 10ns, and the signal overdrive below 25ns, which allows to efficiently detect hits in two consecutive bunch crossings.

4.2.3 Optoelectronic Transmission

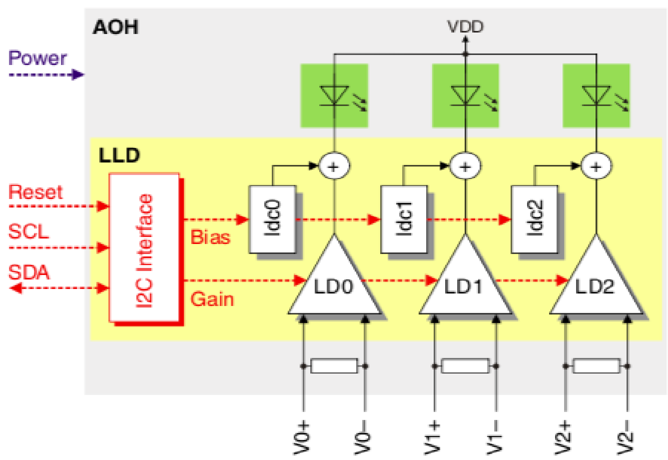

FIGURE 4.6 – Block diagram of the Analog Optohybrid and the Linear Laser Driver

The analog signal is transmitted from the inner detector to the back-end electronics using the Analog-Opto-Hybrids (AOH). A Digital-Opto-Hybrid (DOH) is used to control and configure the AOHs via I2C interface. The ASICs' output signal is driven as AOH input signal and is therefore converted into a proportional current, to wich an adjustable offset is added [14].
Each AOH provides 3 channels equipped with laser diodes with ajustable bias current and gain. The laser diodes are driven by the Linear Laser Driver (LLD) [15] which essentially translates the differential input voltage into a suitable drive current. It has four selectable gains and an adjustable bias (offset) current to tune the light output range. The LLD is controlled by its I2C interface, where gains and bias currents can individually be set for each of the three channels. The current is then converted into infrared light at wavelenght of 1310 nm which is sent via a 80m long singlemode fibre in pulse-amplitude-modulated format (PAM). The optical signal is then received and converted into an electrical signal by an ARx12 optical receiver.

4.3 Back-End Systems

As shown in Figure 4.7, the current BCM1F back-end is based on two systems : CAEN VME and MicroTCA. The objective is to then migrate to a full MicroTCA back-end system in order to achieve a better time resolution thanks to the high MicroTCA sampling rate [16].

4.3.1 Versa-Module-Eurocard (VME)

The CAEN VME system is the main system used during Run2 operation. It allows for luminosity measurement using a constant threshold discriminator and a realtime histogramming unit with 6.25ns time resolution. This system was not used in the test beam campaign that will be discussed in the coming chapters.
The VME ADC is a set of CAEN ADC digitizers V1721 [17] with 8 channels per board. The 8 bit ADC operates at a 500 MS/s samplig rate, equivalent to a 2 ns sampling time. The modules include a front panel clock input and a phase-locked loop (PLL) for clock synthesis from internal/external references. In order to synchronize the system with the LHC clock, the ADCs were customized by CAEN to be able to lock on the 40.08 MHz LHC clock. They allow for detector commissioning and efficiency monitoring. Samples are stored in a ring buffer according to an event structure and the ADCs are then read out via optical links.

4.3.2 Micro-Telecommunication-Computing-Architecture (μTCA)

The MicroTCA technology [18] is developped for advanced signal processing that is implemented in FPGA. It is chosen for the upgrade and still in development. It consists of high speed analog-to-digital converter FPGA Mezzanine Cards (FMC) mounted on Advanced Mezzanine Card (AMC) carrier boards. The system is controled by the NAT MicroTCA Hub Module (MCH). The dedicated FMC125 is a four channel ADC FMC card hosting an E2V EV8AQ160 8-bit quad ADC with a sampling rate up to 1.25 GHz. The ADC channels output the ditigized data on a 16-bit Double Data Rate LVDS bus at half the sampling frequency. The main advantages of the MicroTCA system is providing advanced peak detection, higher resolution timing histogram and high statistics amplitude histograms for fast efficiency tracking.

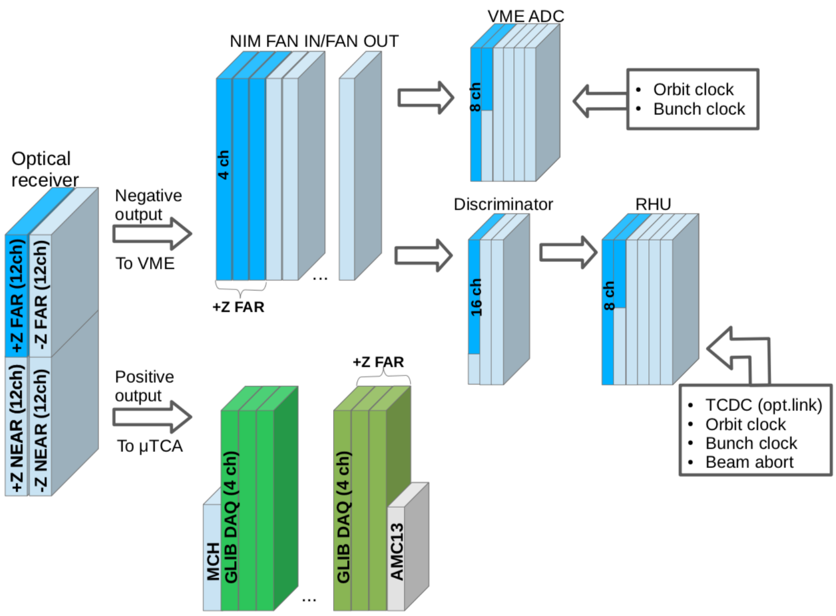

FIGURE 4.7 – Schematic view of the BCM1F backend systems [5]

5 Test-Beam Setup

In order to test the newly developed silicon sensors and the integration with front-end chain of BCM1F, a prototype consisting of sensor, front-end ASIC and optical transmission was tested at the DESY II test-beam area using an electron beam. In this chapter, the test-beam area and the various components used during the test beam campaing are presented.

5.1 Test-Beam Area

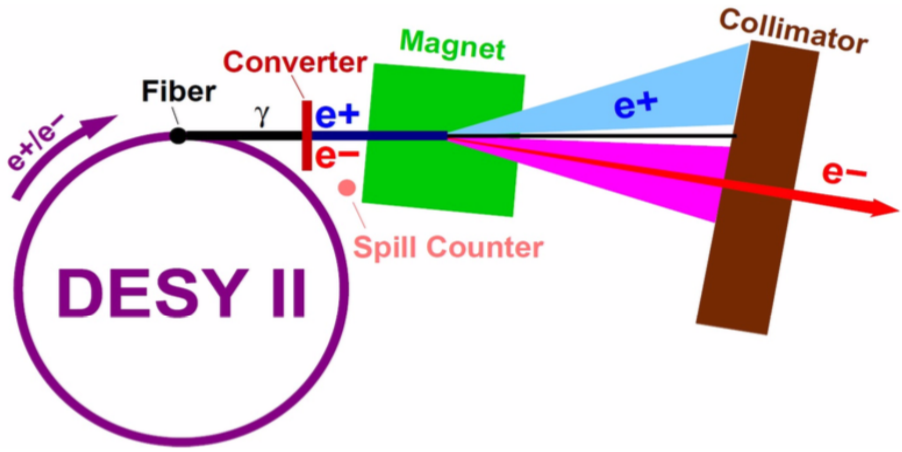

FIGURE 5.1 – Description of the test-beam area at DESY

DESY operates a test-beam facility with three test-beam lines (21, 22, 24). The electron or positron beams are provided through the conversion, on a carbon fiber target, of the DESY II electron or positron Bremsstrahlung radiation. The beams can contain up to 1000 particles per cm^2 of an energy from 1 GeV to 6 GeV. The energy loss of electrons within this energy range is within approximately 10% equal to a MIP. A description of the test-beam area is shown in Figure 5.1. For the BCM1F test-beam, the energy was set to 5.4GeV. The rate was about 80Hz and the beam size 8x8mm^2.
In addition to the electron beam, the test-beam facility provides a EUDET-type pixel beam telescope [19] for the track reconstruction. Two arms of 3 planes are positioned and centered along the beam axis. In between the two telescope arms, a XY movable stage with mm precision is provided In order to control the position of the device-under-test (DUT) with respect to the beam. Four Hamamatsu Photo-Multiplier Tubes (PMTs) with appropriately sized plastic scintillators are included in the test infrastructure. Two of them are positioned in front of the telescope, and the other two are positioned in the back to trigger on particles passing the telescope. A schematic of the test-beam setup, including the telescope plane, the scintillators and the DUT is shown in Figure 5.2 .

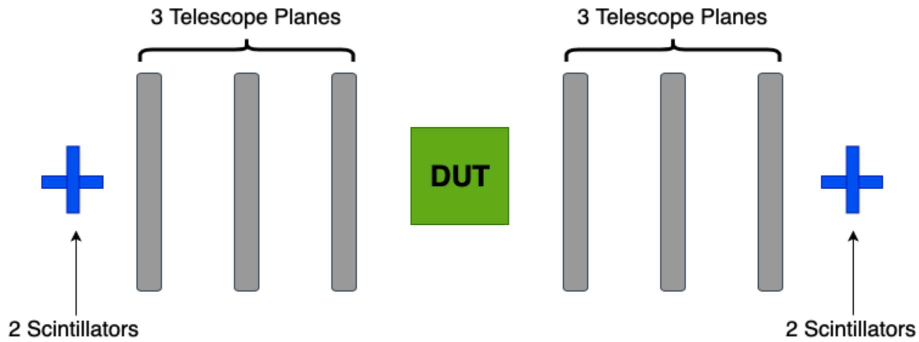

FIGURE 5.2 – Schematic of the test-beam setup

Several devices and computers were used for the data taking. The signals of the four scintillators are fed to the Trigger Logic Unit (TLU) that outputs a logic "AND"of all four input signals and a trigger number [20]. The information is then distributed to the telescope and DUT readout systems in order to trigger the data acquisition. The TLU offers a trigger-data-handshake mode which takes into account feedback from the connected DUT and telescope planes and asserts a busy state to block new incoming triggers and only sends a new one if all devices are not recording anymore. This allows for synchronization of the data acquisition. Figure 5.3 shows the complete trigger scheme and the data acquisiton chain used for the test-beam.

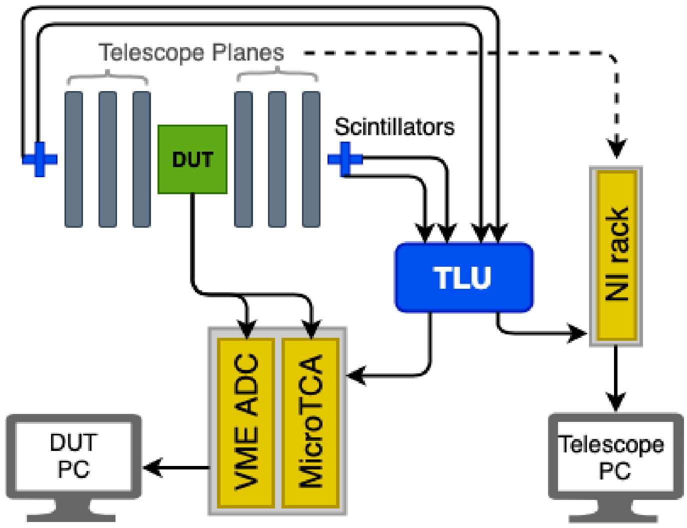

FIGURE 5.3 – Trigger and data acquisition scheme used during the test-beam

The telescope planes are connected to a National Instruments (NI) readout rack including dedicated NI readout modules and data is processed with NI FlexRIO FPGAs. The data is then transmitted via Ethernet to a Telescope computer. The DUT is connected to a readout rack where the two back-end systems are located. First, the crate holds a CAEN v1721 ADC that receives the trigger signal from the TLU, but doesn't operate on the hand-shake mode. Second, the crate holds the MicroTCA system which is connected to the TLU via a Register Jack type (RJ45) connector on which the trigger signal is sent and that allows the system to operate on the hand-shake mode. A DUT computer reads out the CAEN v1721 ADC and the MicroTCA data.
As a final step, both the Telescope computer and the DUT computer send the data to an external computer for further processing through the test-beam data acquisition software framework that will be presented in Chapter 6.

5.2 EUDET-type Pixel Beam Telescopes

The telescopes used are EUDET-type pixel beam telescopes [21] which allow to track the test beam particles. They have been developed to meet most user requirements in terms of easy integration of the device under test (DUT), precise spacial resolution and suitable event rates. As mentioned before, the EUDET telescope consists of two telescope arms each composed of three planes. Each plane is a MIMOSA-26 monolithic active pixel sensor with a pitch size of $18.4\mu m \times 18.4\mu m$ and a pixel arrangement of 1152 columns and 576 rows, which results in an active area of about $21.2mm \times 10.6mm$. With a thickness of $50\mu m$ silicon and a $25\mu m$ thick Kapton foil shield, the sensor is protected from environmental light and the material budget is kept low in order to achieve high track resolution at 1-6 GeV/c. However, the realistic track resolution depends on the beam energy, the plane spacing and the material budget of the DUT.

5.3 Device Under Test

The Device Under Test is the BCM1F Test Board, a simplified version of the BCM1F detector C-shaped module. It is a $14cm \times 14cm$ PCB mounted with two $200\mu m$ and $300\mu m$ $1.7mm \times 1.7mm$ AC-coupled double diode Silicon sensors together with a dedicated BCM1F readout ASIC. Wire bonds connect the sensor pads to the chip inputs. High-voltgage and low-voltage (2.5V) inputs are integrated to the board for sensor bias and ASIC powering, respectively. Several potentiometers are present on the board allowing different ASIC configuration (shaper offset, pre-amplifier, ...). Three LEMO cable inputs are also added for test pulse configuration and injection to allow calibration of the detector. Finally, four high performance differential outputs are provided and can be further fed to the AOH inputs for signal transmission.

The optical transmission of the signal to the backend electronics is done through the Opto-board. It is a long rectangular PCB on which four AOH connectors are mounted. An additional connector is dedicated to the DOH that handles configuration of the AOHs. The optical fibers are merged together in a 12-fiber MPO cable that is connected to an analog optical receiver used to convert the optical signal into an electrical signal. The converted signal is then fed to the data acquisition systems for further processing and saving.

The read out chain used during the test-beam campaign is the same as the one designed for BCM1F to be installed in the CMS cavern.

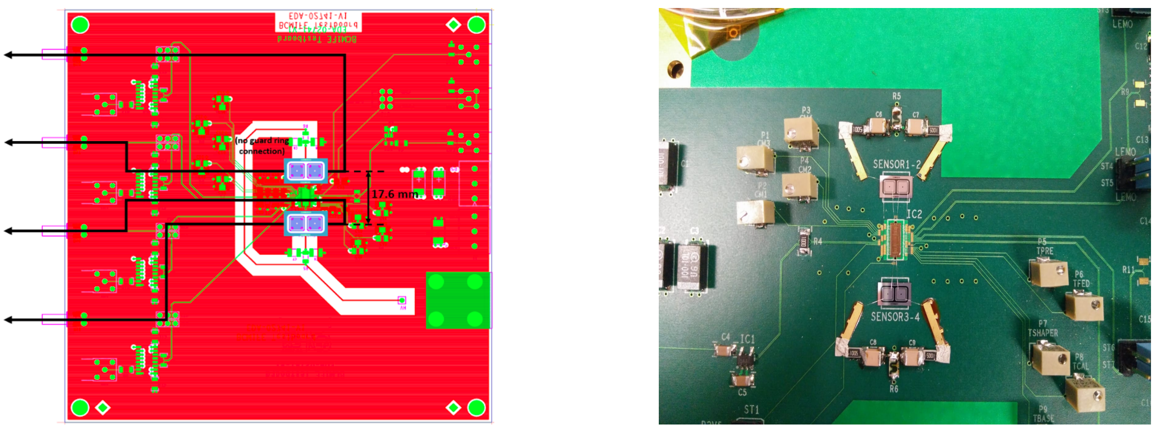

(a) Sketch of the BCM1F Test-Board | (b) Picture of the BCM1F Test-Board

FIGURE 5.4 – Sketch (a) and picture (b) of the BCM1F Test-Board with the mounted silicon sensors and the BCM1F ASIC

Each of the sensors diodes is equipped with a guard-ring. In order to study its effects on the detector performance, the latter was grounded on the $200\mu m$ sensor, while it was kept floating on the $300\mu m$ sensor. Each sensor diode was connected to a dedicated outputs of the test-board. On `Sensor1`, which is the $200\mu m$ sensor with the grounded guard-ring, the diodes were connected to channels 0 and 1. On `Sensor2`, which is the $300\mu m$ sensor with the floating guard-ring, the diodes were connected to channels 2 and 3. A channel mapping with the related sensor information is given in the Table 5.1.

Sensor	**Channel**	**Thickness** $[\mu m]$	**Guard-Ring**
2	0	300	floating
2	1	300	floating
1	2	200	grounded
1	3	200	grounded

Table 5.1 – Test-Beam channel mapping and related sensor information

Moreover, a plastic box with red LEDs is used to expose the sensors to additional light and thus inject a controlled amount of leakage current to simulate effects of radiation damage. The DUT was positioned perpendicular to the beam. A picture of the test beam setup with the integrated DUT (tilted at 45°) is shown in Figure 5.5.

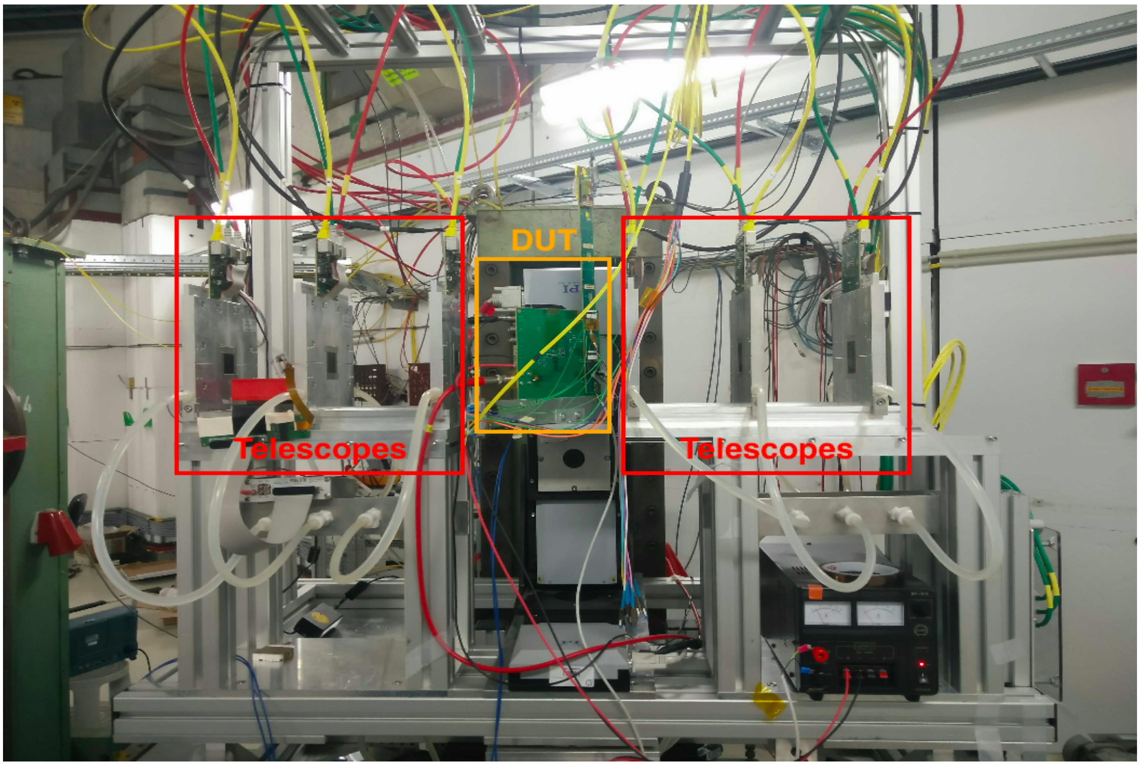

Figure 5.5 – Picture of the test beam setup with the telescope planes (red box) and the integrated DUT (orange box)

6 Test-Beam Data Acquisition

6.1 EUDAQ Software Framework

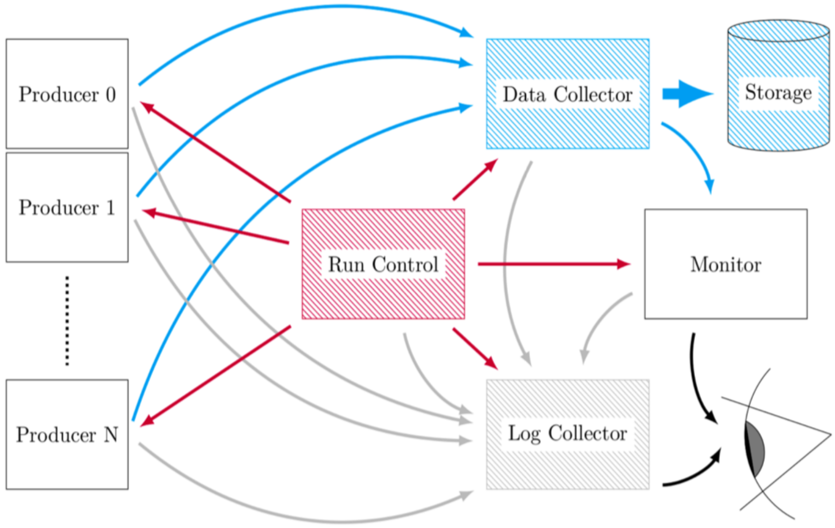

FIGURE 6.1 – EUDAQ Software Framework block diagram [22]

The test-beam data acquisition is based on the EUDAQ Software Framework [22]. It is a modular platform framework that serves as data taking environment for the EUDET-type beam telescopes, and that allows an easy integration of external data acquisition systems. It is based on completely independent modules communicating via TCP/IP, and is designed for synchronous data acquisition systems. It requires one event per trigger per integrated data acquisition system before building the global event.
The main modules included in the EUDAQ Software Framework are shown in Figure 6.1 and are as follows :

Run Control

The central part of the framework is the `Run Control` and its graphical user interface (GUI) shown in Figure 6.2. It controls and ensures communication between all the framework subroutines. The GUI provides all controls necessary to initialize, start and stop a data acquisition run.

Producers

The detector data are delivered to the framework by the so-called `Producers` when a trigger occurs. These are the modules that link the various data acquisition systems to the EUDAQ framework. Through theire library interface with the EUDAQ framework, they provide a set of commands that are called by the `Run Control`. This allows for an easy integration of external user data acquisition systems as desribed in Section 6.2.

Data Collector
The data read out by the `Producers` is then streamed to the so-called `Data Collector`. The `Data Collector` is responsible of the event building, and storage in binary files of the merged data streams.

Log Collector
The `Log Collector`, with a dedicated GUI, gathers logging information for each run from all subroutines, displays them and saves them in a log file.

Online Monitor
The `Online Monitor` tool provides a way to ensure data quality checks during data acquisition. It is connected to the Data Collector and requests a fraction of the collected data, decodes it, and builds basic plots such as hit maps or correlation plots.

Data Converter-Plugin
The data decoding is performed using the `Data Converter Plug-Ins` for each data acquisition system connected to the `Run Control`. The plug-in to be called is deduced by the event type transmitted by the `Producer` and written to the data stream by the `Data Collector`. Each `Data Converter Plug-In` can implement conversion to various data format such as the EUDAQ format used by the `Online Monitor`, ROOT trees, or to LCIO format which is used by the offline reconstruction software EUTelescope.

Configuration files
The acquisition environment is configured via global configuration files. Each individual module has its own information parsed and distributed by the `Run Control`. The configuration file is a plain text file divided into sections dedicated to each individual module, which contains a set of parameter-value pairs defined for the module.

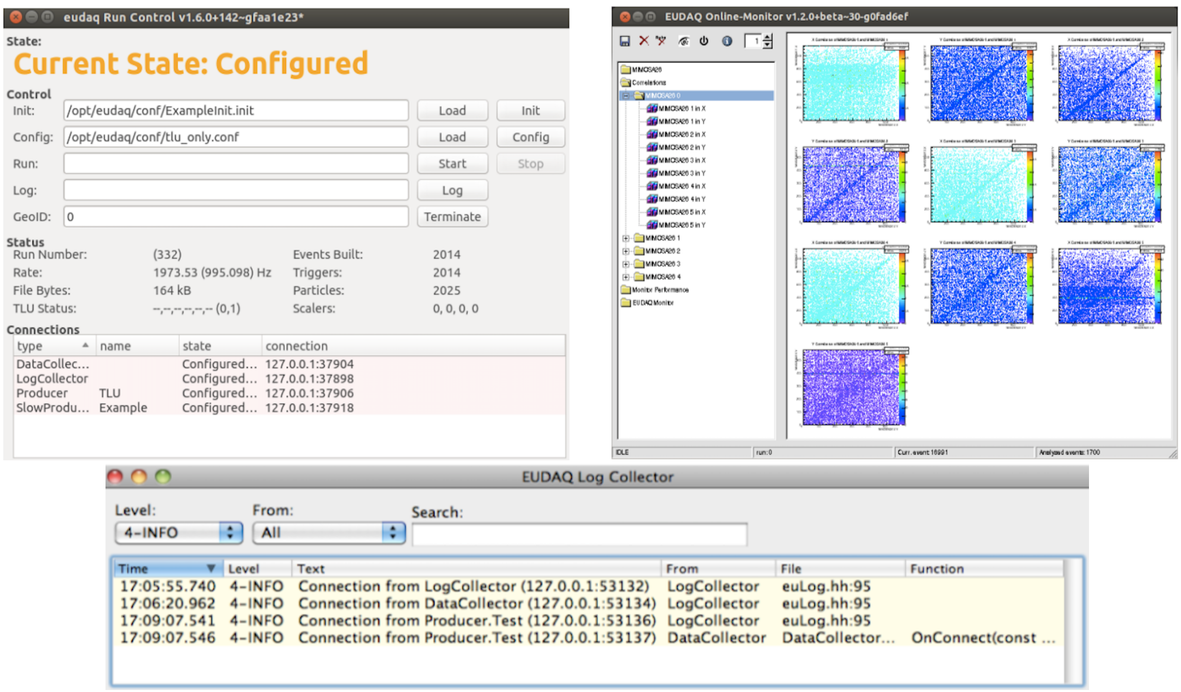

FIGURE 6.2 – EUDAQ Graphical User Interface including the RunControl (top-left), the OnlineMonitor (top-right) and the LogCollector (bottom) [22]

.

6.2 BCM1F Data Acquisiton Systems Integration

In order to have a unified data taking scheme during the test-beam campaing, `VME` and `MicroTCA Producers` as well as dedicated `Data Converter Plug-Ins` were implemented and included into the EUDAQ Software Framework. In addition to the mentioned modules, the default `Online Monitor` was modified in order to include specific plots related to the BCM1F detector. The various implementations are describe in this section.

6.2.1 VME and MicroTCA Producers

The `VME` and `MicroTCA Producers` are the binding parts between BCM1F data acquisition systems and the central `EUDAQ Run Control`. They consist of `CommandReceivers` and `DataSenders`. The first receives commands from the `Run Control` while the latter sends binary events data to the `Data Collector`. The implemented `BCM1F Producers` inherit from a `Producer` base class provided in order to simplify the integration. They are linked to the VME and MicroTCA libraries and compiled against the EUDAQ library containing all of the required communication over the network.
Each of the `Producers` is a set of four virtual methods inherited from the `Producer` base class : `OnInitialise(), OnConfigure(), OnStartRun(), OnStopRun()`.

OnInitialise() : This method is called when the *Initialise* button is pressed in the `Run Control` GUI. It reads a **.init* file and extracts the parameter-value pairs related to the concerned system. For the VME system, this method performs the search and acknowledgement of the VME ADCs in the VME crate using a base address [23], while for the MicroTCA system it is in charge of assiging an IP address to the AMC GLIB card through IPMI commands implemented in the MicroTCA libraries [24].

OnConfigure() : This method is called when the *Configure* button is pressed in the `Run Control` GUI. It reads a **.conf file* and configures the related systems using the dedicated parameter-value pairs. For the VME system, it configures parameters such as the acquisition window or the channel mask using the `CUSTOMSIZE` and the `CHANNELMASK` registers, respectively. For the MicroTCA system, the configuration consists of setting up the trafic to the AMC GLIB card, configuring the FPGA thresholds, and performing various functional checks on the AMC GLIB card. All details related to the initialization and configuration of both the VME and the MicroTCA systems can be found in references [23] [24] .

OnStartRun(), OnStopRun() : These methods are called when the *Start* or *Stop* button is pressed in the `Run Control` GUI. The data acquisition is then started or stopped on both systems.
Both the `VME` and the `MicroTCA Producers` were implemented such that a whole signal waveform captured in a specified acquisition window is saved and sent to the `DataCollector`.

6.2.2 VME and MicroTCA Converter Plugins

A converter plugin, included afterwards in the EUDAQ Plugin Manager, has ben implemented for each of the BCM1F data acquisiton systems. They are used by the EUDAQ Data Handlers to convert raw data sent by the Producers into `Standard Event` format, a EUDAQ specific format that is mainly used in the Online Monitor, or into the LCIO format, which is the format used in the EUTelescope analysis framework.
For each run event, one `StandardEvent`, inheriting from the `Event` base class, is created that

contains data from the whole telescope and any integrated DUT. A run will therefore consist of a sequence of `StandardEvents`. Within the latter, the decoded telescope and DUT data are stored in an array of `StandardPlanes`, each representing one sensor plane of the telescope, or one sensor diode of the BCM1F detector. Therefore, each telescope `StandardPlane` contains the charge values extracted from pixels of one sensor plane, while for the BCM1F detector each `StandardPlane` contains the full waveform extracted from every sensor channel.

6.2.3 BCM1F Online Monitor

As the provided default `EUDAQ Online Monitor` doesn't include some specific plots related to the BCM1F detector, the monitor source code was extended by adding the needed plot content.
The `Online Monitor` content is managed by a histogram class that handles each `StandardEvent` within a run, creates and fills useful histograms. The histograms are then handled by a Collection class that is in charge of adding them to the `Online Monitor` graphical interface.
The modification of the `Online Monitor` therefore included adding a `BCM1F Collection` class which inherits from a `Collection` base class that provides virtual methods allowing the integration of the plots within the monitor graphical interface. Finally, a `BCM1F Histograms` class was implemented in order to create and fill the needed histograms. The latter takes each `StandardEvent`, extracts the `StandardPlane` corresponding to every detector channel/diode, and provides amplitude spectrum histograms.
A picture of the implemented interface is shown in Figure 6.3. The figure shows amplitude spectra built from two channels of both the VME and the MicroTCA data acquisition systems where each of the waveform samples is binned in the histogram. However, a peak finder function was also included in the code in order to obtain plots containing only peak amplitude values.

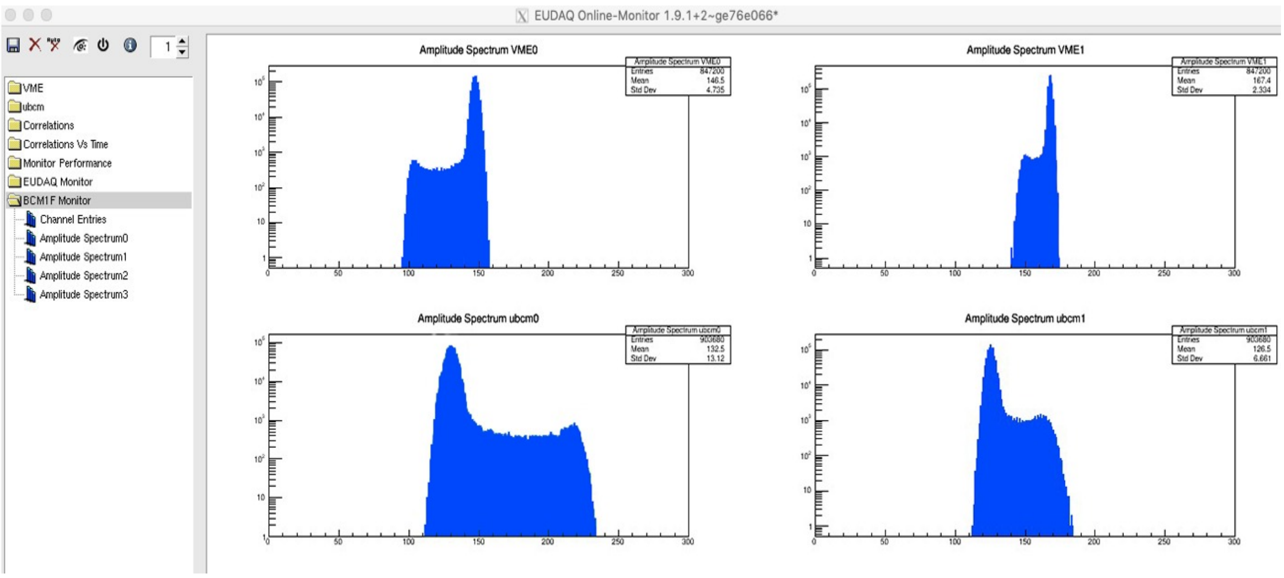

FIGURE 6.3 – Extended EUDAQ Online Monitor including BCM1F histograms

7 Test-Beam Offline Analysis

7.1 Telescope Track Reconstruction

In order to make use of the telescope data, a simplified track reconstruction software implemented by a member of the CMS-DESY group was used. The software exploits the EUDAQ raw data files to extract telescope planes information and build the particles trajectories from the sensor hit positions. It is based on two main processes : The first one is a pre-alignment process that ensures the alignment of the telescope planes and produces a dedicated alignment file. The second one is a post-alignment process that builds the track position using the previously generated alignment file, and that was extended to produce ROOT Trees containing the track informations together with the DUT data. The track reconstruction workflow is described in this section.

7.1.1 Clustering - Hit Making

When a particle traverses a sensor, it very often induces signals in more than one pixel. The first step towards track building is therefore searching for hit pixels that are grouped into clusters. In the software used, the clustering is based on a next-neighbour topological clustering algorithm.
Every hit pixel is in the first place considered as a cluster seed. The cluster is then let growing by determining the number N of neighboring hit pixels ignoring the diagonal neighbors. The pixels included in one cluster are then excluded from the next cluster construction. In addition, an arbitrary criteria was used to reject certain pixels as noisy if they happen to fire over the run more than a threshold set as $NEvents/128$, where $NEvents$ is the total number of events in the run. Once the cluster is built, its center is calculated using a weighted average based on the number of neighbors associated to every pixel of the cluster. Figure 7.1 shows some cluster types examples and the calculation of their weighted center.

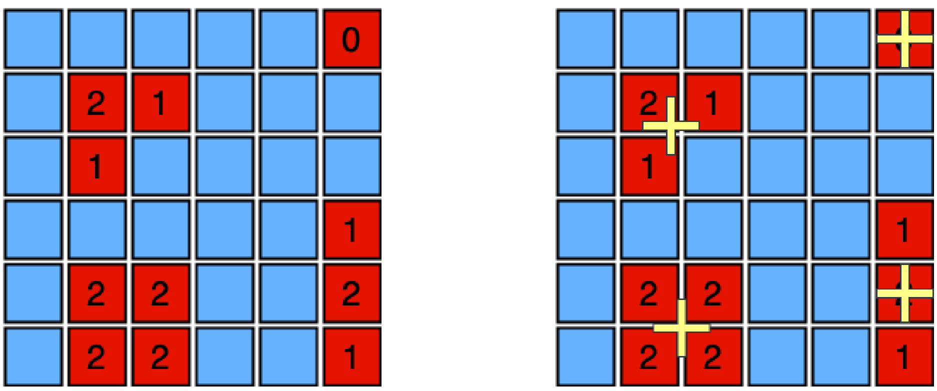

Figure 7.1 – Ilustration of different cluster types with the neighbor weighting (left) and the position of the cluster center (right)

7.1.2 Telescope Planes Alignment

The telescope planes alignment is done in a 3-iteration step. First, initial alignment parameters (shifts, rotations) for each plane are used to convert cluster local positions into global coordinates. Assuming straight line tracks, these clusters are spatially correlated between individual planes independently for both the up-stream and down stream telescope arms. From the considered planes, x and y residual histograms are produced using clusters that have a distance below a defined threshold. Deviation from the zero value of the histogram mean can be interpreted as misalignment. Histograms are then fitted using a gaussian distribution and xy shift parameters are extracted for each of the planes. In addition, the residuals $dx(dy)$ as a function of $y(x)$ are depicted. The slope of these distributions can be exploited in order to extract the rotation parameters around the z axis. An example of the fitted histograms is shown in Figure 7.2. The process is iterated 3 times for each plane in order to achieve finer alignment values.

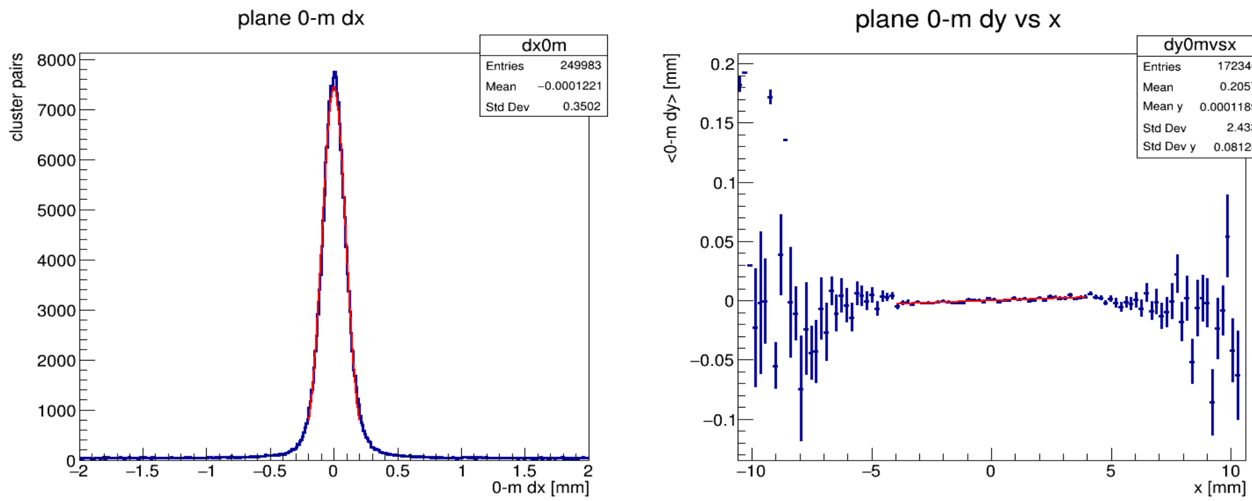

FIGURE 7.2 – Fitted x-residuals histogram (left), and y-residuals as a function of x (right) using clusters from planes 0 and 1

7.1.3 Track Building

To build the telescope tracks, the software uses a simplified algorithm based on three main assumptions :

- all telescopes are parallel to each other
- the incoming beam is perpendicular to the telescope planes
- multiple scattering is negligible and thus not considered

The reconstructed tracks are therefore straight lines built over 3 steps using each planes produced clusters. In the first place, straight cluster lines are built from the up-stream arm content considering a circular search region of $100\mu m$ radius. So-called `triplets` are then saved with their associated xy position and slope. The same procedure is applied to the down-stream telescope arm in order to save so-called `driplets` with their related information. Finally, both `triplets` and `driplets` are extrapolated to the DUT position using the setup geometry information, and the matching ones within the search region are used to produce straight line tracks. The mean value of the `triplet` and `driplet` xy positions is taken as the final track position. Figure 7.3 shows a sketch of the telescope `triplet` and `driplet` used to build a track.

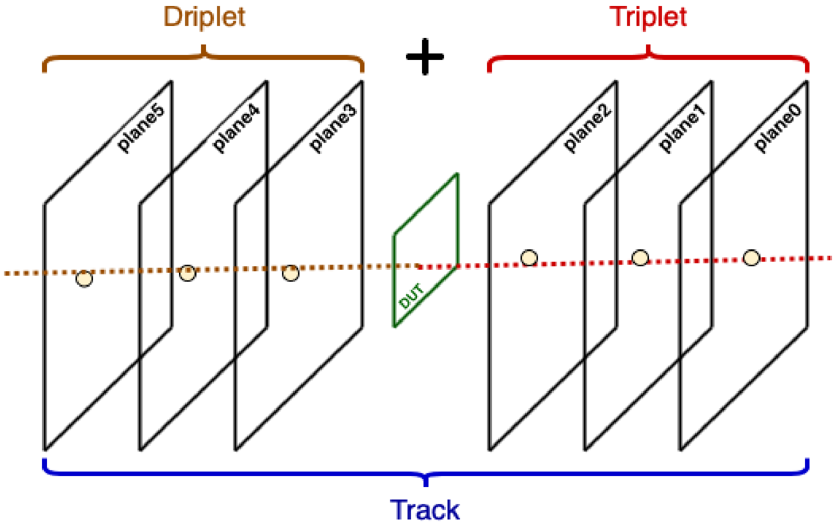

FIGURE 7.3 – Sketch of telescope `triplet` (red) and `driplet` (brown) used to build a track.

7.1.4 Track Reconstruction Results

Figure 7.4 shows the number of reconstructed tracks from a run of 163841 triggers. 10% of the triggered telescope data are subject to multiple track reconstruction. These are events triggering one event but producing more than one reconstructed track. However, in around 40% of the events no track is reconstructed. The latter effect is most likely due to track multiple scattering caused by the important material budget introduced by the BCM1F detector, and that is not taken into consideration in the track reconstruction algorithm as tracks are assumed to be straight lines.

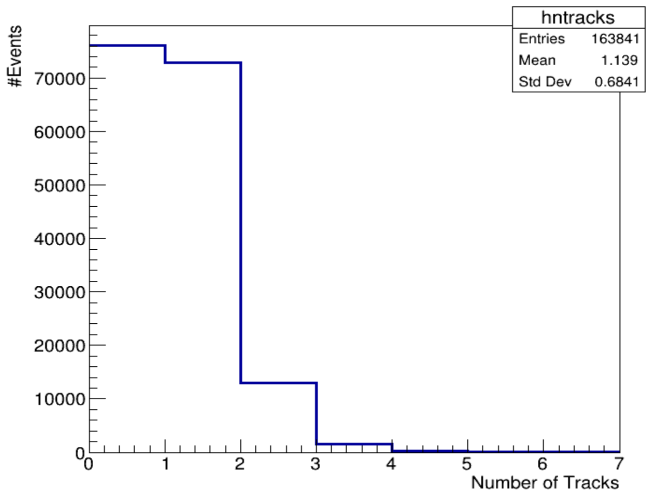

FIGURE 7.4 – Number of reconstructed tracks for all triggered telescope events

Figure 7.5 shows the distribution of the particle impact positions in x- and y-direction of the triplets built from the up-stream arm of the telescope. A flat beam density distribution is observed in the ranges from -5mm to 3mm in x-direction and from -4mm to 4mm in y-direction, which almost corresponds to the expected beam size of 64mm^2. The sharp drops at the edges of the distributions are related to the limits of the active telescope area of 21×10.6 mm^2.
In order to ensure a unique correspondence between signal in the DUT and particle impact position, only events with one reconstructed track should be selected. Since the silicon metallization area is around 4×4 mm^2, only around 20% of the triggered events are expected to

provide tracks hitting the sensitive sensor area, from which about 10% are excluded due to multiple track reconstruction.

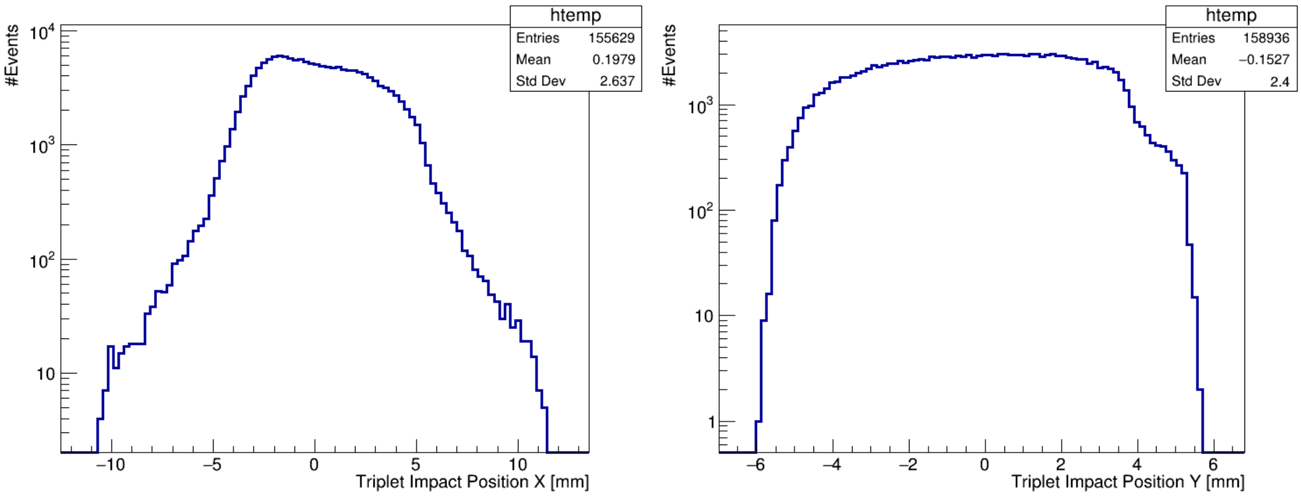

FIGURE 7.5 – Distribution of the triplet impact positions in the x-direction (left) and the y-direction (right)

7.2 Signal Amplitude Spectra

During the test-beam campaign, raw data acquired by both the VME and MicroTCA systems consisted of full signal waveforms read and saved from the four connected sensor channels/diodes when a trigger was received from the TLU. The first part of the test-beam analysis was performed using only the BCM1F detector data and omiting the telescope data. An example of a MicroTCA pulse waveform and some of the related pulse features used in the analysis are shown in Figure 7.6.

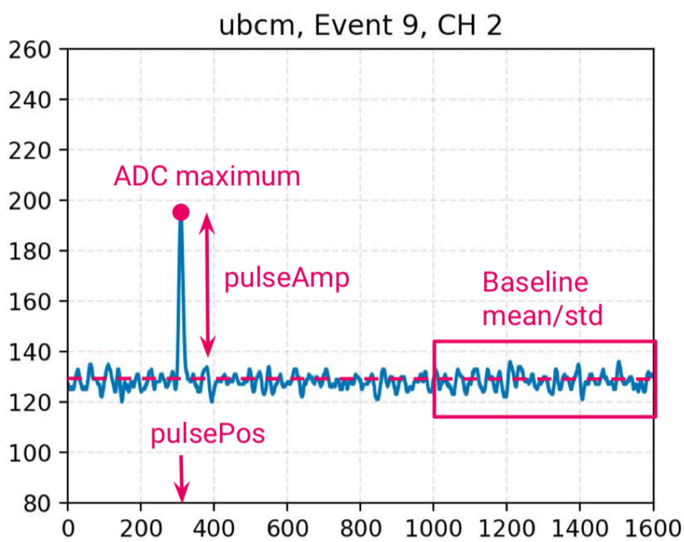

FIGURE 7.6 – Example of a MicroTCA pulse waveform and its pulse features

The pulse features include the pulse peak, the peak position, the baseline mean and standard deviation, and the pulse amplitude calculated as the baseline substracted peak value. The same information was used for the VME system with the difference that the peak has an opposite polarity as the optical receiver is differential and the positive half waves are used by the

MicroTCA system while the negative ones are fed to the VME system.

For each of the considered events, the signal amplitude analysis calculates first the baseline mean and the baseline standard deviation by filling a histogram of a number N_B of ADC values outside the expected pulse region. The histogram is then fitted with a gaussian distribution to extract the baseline mean and standard deviation. Afterwards the pulse amplitude is calculated by looking for the maximun(minimum) ADC value over the whole ADC samples from the MicroTCA(VME) data :

$$\begin{aligned} MicroTCA\ Signal\ Amplitude &= |\ Maximum\ ADC\ Value - Baseline\ Mean\ | \\ VME\ Signal\ Amplitude &= |\ Minimum\ ADC\ Value - Baseline\ Mean\ | \end{aligned} \tag{7.1}$$

Using the previously calculated pulse amplitude, an amplitude spectrum was produced for each sensor using both the VME and MicroTCA data. As mentioned in Chapter 3, the energy loss distribution of the electron beam particles in silicon sensors follow a Landau distribution. The amplitude spectra were therefore fitted on a specific window using a Landau distribution convoluted with a gaussian distribution in order to account for the electronic noise. Figure 7.7 shows amplitude spectra of Sensor1 ($200\mu m$) and Sensor2 ($300\mu m$) using one channel data from both VME and MicroTCA systems.

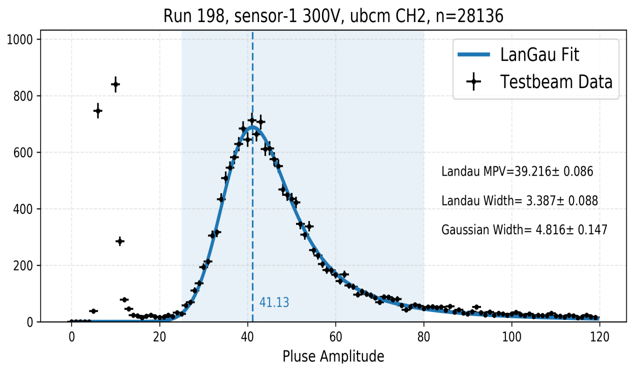

(a) MictroTCA, Sensor1, $200\mu m$, CH2

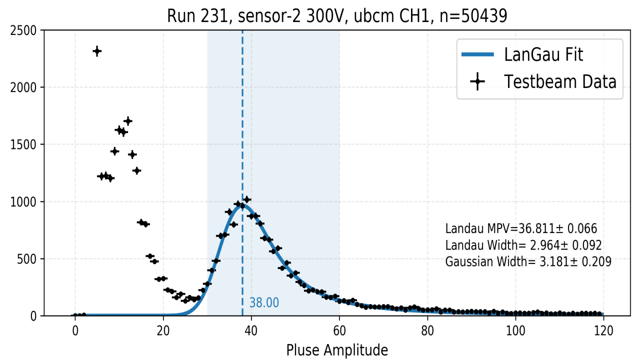

(b) MicroTCA, Sensor2, $300\mu m$, CH1

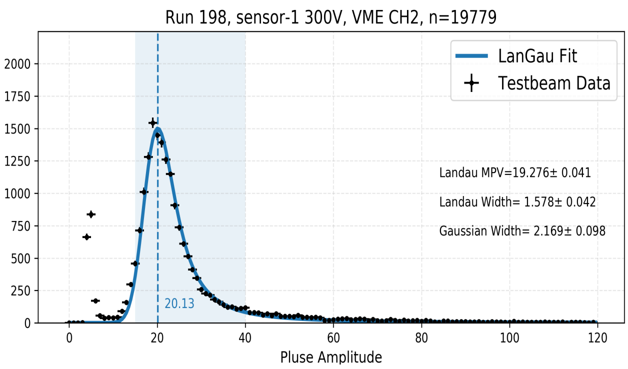

(c) VME, Sensor1, $200\mu m$, CH2

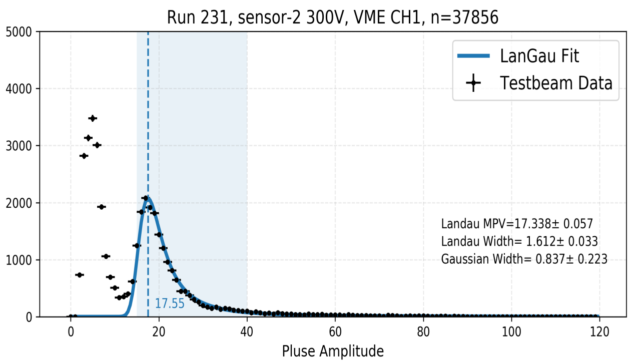

(d) VME, Sensor2, $300\mu m$, CH1

FIGURE 7.7 – Sensor1 ($200\mu m$) LanGauss fitted amplitude spectrum

The blue shadow represents the selected range to be fitted. The `Landau MPV` and `Landau Width` parameters are the Landau location μ and scale c parameters described in Equation 3.2 and extracted after the fit, while the `Gaussian Width` parameter is the standard deviation σ of the convoluted gaussian distribution. The apparent error bars represent the absolut uncertainty of the bin content that scales as $\sqrt{N}$.

Results from the two back-end systems depicted in Figure 7.7 show that as the dynamic range of the VME system is twice the MicroTCA one the amplitude spectrum Most Probable Value (MPV) given by VME is half the one provided by MicroTCA. Moreover, the higher value of the σ parameter in MicroTCA is due to a noisier system and yields a higher c parameter value and thus a larger and more spread Landau distribution.

Considering differences between Sensor1 and Sensor2, Figure 7.7 shows that the separation between the signal and noise is much better on Sensor1 that has the guard ring grounded. This is most likely due to the fact that a floating guard ring, under high voltage, extends the electrical field above the edges of the metalisation area. The sensor then becomes sensitive to particles hitting the edges where the electrical field is distorted and thus low amount of charges is collected. Consequently, events in the low range of amplitude values that are represented by a non-zero separation region or a spectrum shoulder, as shown in Figure 7.7b, are introduced. This effect will be demonstrated further using the telescope data.

7.3 Detector Calibration

When a particle traverses one of the diodes, the BCM1F ASIC converts the induced sensor charge Q_{Signal} into an output voltage V_{Signal} that is measured with an ADC and represented by the calculated amplitude A with $Q_{Signal} \propto A$. A calibration procedure is therefore essential to extract the calibration factor k needed to transform the ADC pulse amplitude into an equivalent measured charge :

$$Q_{Signal} = k \cdot A \tag{7.2}$$

To extract the calibration factor k, the BCM1F test-board provides a circuit, as shown in Figure 7.8, allowing for constant charge injection into the ASIC input. The amount of charge injected Q_{Cal} is controlled by the amplitude of a calibration pulse V_{Cal} fed into the ASIC channels by a capacitance C_{Cal}. The signal is then amplified in every ASIC channel and sent through the corresponding optical line to be digitized by the VME and MicroTCA ADCs.

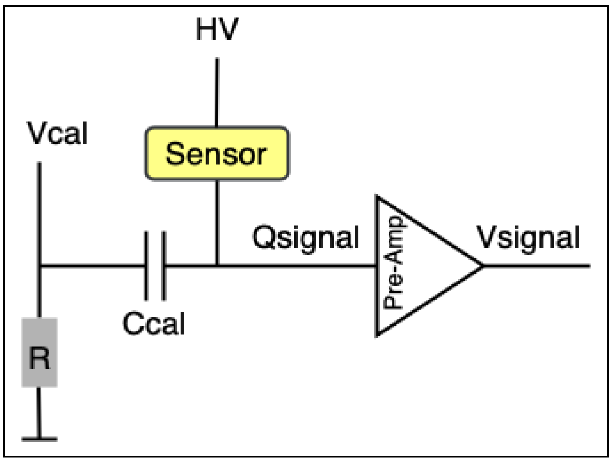

FIGURE 7.8 – Schematic of the calibration circuit for the BCM1F detector calibration

A scan over an injected charge ranging from $1fC$ to $8fC$ was performed for all four channels. For the calibration to be convenient to further analysis, the pulse amplitude value was measured as a function of the injected charge converted into number of electrons. The calibration constants were then extracted for each channel of the two back-end systems using a linear fit. Figure 7.9 shows the fitted pulse amplitudes measured as a function of the injected charge.

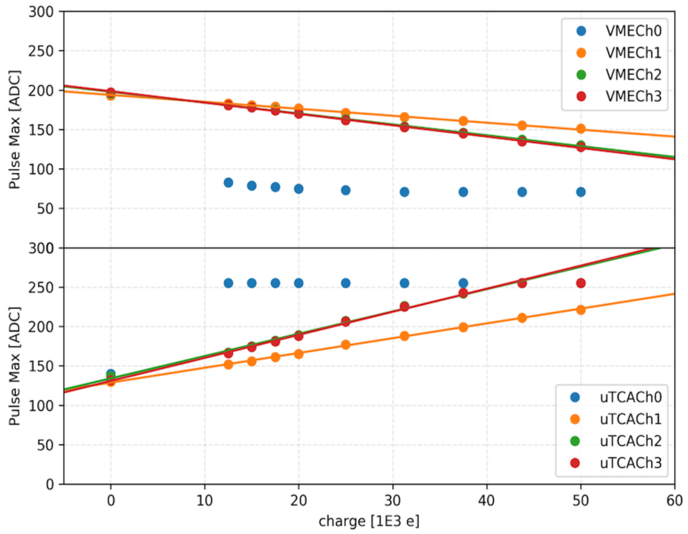

FIGURE 7.9 – Pulse amplitude measured from VME and MicroTCA systems as a function of the injected charge converted into number of electrons

Figure 7.9 shows that both VME and MicroTCA systems saturate on CH0, which means that no calibration is possible on this channel. Therefore it was excluded from the fit and only calibration constants of the remaining channels were extracted. The latter are given in Table 7.1.

Channel	VME CH1	VME CH2	VME CH3	uTCA CH1	uTCA CH2	uTCA CH3
k [e^-/ADC]	1133.6	724.1	695.7	532.8	353.1	341.8

TABLE 7.1 – Calibration factor k for channels of both back-end systems

7.4 Sensor Effective Thickness

The sensor effective thickness is a sensor feature that provides an information about how much of the actual sensor thickness is contributing to the signal generation. It can be determined by considering the number of electron-hole pairs created per thickness unit (μm) in silicon sensors by Minimum Ionizing Particles (MIPs) and convert the most probable number of electrons measured in the BCM1F sensors test beam runs into a related effective thickness.

The analysis objective was to provide the sensors effective thickness as a function of applied high voltage. A high voltage scan was therefore perfomed for each sensor and measurements were made with respect to each associated channels. High voltage ranges from 50V to 500V for Sensor1, and from 100V to 800V for Sensor2. Excluding the non-calibrated CH0 for Sensor2, amplitude spectra were built for each high voltage value and fitted with a Landau Gaussian distribution to extract the MPV value in ADC units. The calibration factors were then used to convert the MPV values from ADC units to an equivalent number of created electrons in the sensor. Finally, the effective thickness was calculated as follows :

$$Effective\ Thickness\ [\mu m] = \frac{MPV[ADC] \cdot k[e/ADC]}{78[e/\mu m]} \tag{7.3}$$

The calculated number of e^-h^+ pairs created per μm by MIPs in silicon sensors was deduced from literature [25] and was taken to be around 78 $e^-h^+/\mu m$. Figure 7.10 shows results of effective thickness extracted from the high voltage scan for Sensor1 and Sensor2.

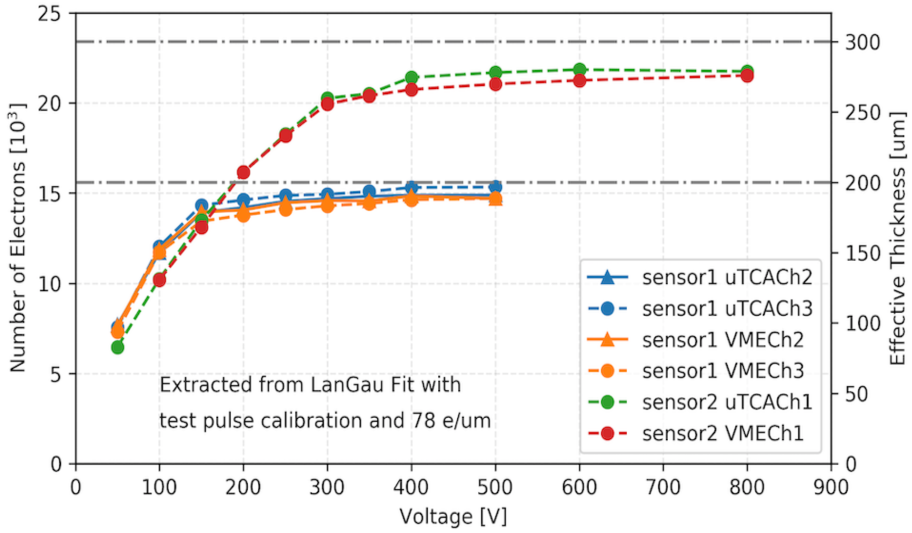

FIGURE 7.10 – Sensor effective thickness as function of high voltage

Figure 7.10 shows that Sensor1 reaches a plateau around 140V while Sensor2 reaches the plateau at around 280V. These values are in agreement with the capacitance measurements made on the mounted sensors that yielded a full depletion voltage value of 140V for Sensor1 and 280V for Sensor2.
Moreover, in full-depletion and over-depletion regimes, Sensor1 shows an effective thickness around 196μm, which represents >98% of the actual sensor thickness. However, for the same depletion regimes, Sensor2 shows an effective thickness around 270μm, which represents approximately 90% of the actual sensor thickness. While a imperfect calibration of Sensor2 channels could be considered as a cause for this effective thickness drop, guard ring effects could also be in cause of it as for Sensor2 the guard ring is kept floating and thus highly affects the electrical field inside the sensor bulk. But this hypothesis needs further investigation using simulations of the electrical field inside the sensor volume.

7.5 Sensor Signal and Particle Impact Position

The objective of this analysis was to include the telescope tracks information in order to perform a position-based study of the sensors. The latter included investigations of the guard ring effects, sensor edge investigation and Charge Collection Efficiency (CCE) measurements as a function of sensor position. However, before being able to perform any of the mentioned studies, synchronisation loss issues presented in this section needed to be investigated and solved in order to provide quality data for the analysis.

7.5.1 The Synchronisation Loss Puzzle

When the analysis of the test-beam data started including the telescope track information, synchronisation loss issues yielded by an important and unexpected sensor efficiency drop were discovered. Both the VME and the MicroTCA systems were concerned by this issue but it appeared to be more critical to the MicroTCA system. The main cause of this effect is not yet determined, but it is suspected to be originating from a misbehaviour of the hand-shake mode in one or more of the test-beam data acquisition systems. Figure 7.11 shows an example of the synchronisation loss in the VME system yielded by a sudden sensor efficiency drop after a certain number of events.

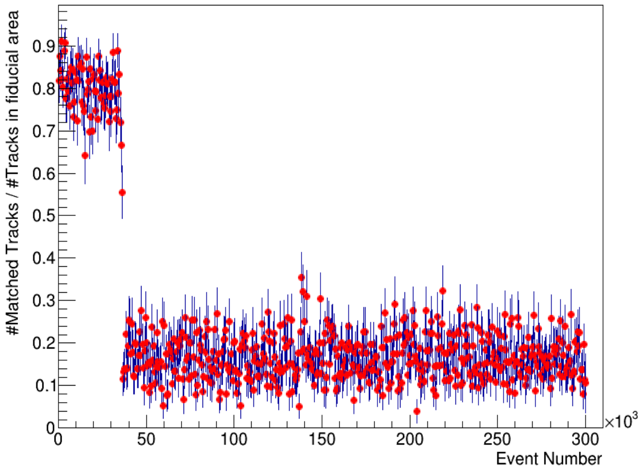

FIGURE 7.11 – Example of the VME system synchronisation loss shown using sensor efficiency

The sensor efficiency, which is the ratio between the number of particles in the sensor fiducial area and the number of particles in the fiducial area matching a signal pulse in the DUT, is calculated for bunches of 500 events over the whole run. The sudden efficiency drop around 40k events clearly indicates a data conflict, most likely an event mismatch between the telescope data and the DUT data.
Investigations and comparision of the telescope and DUT data showed that the synchronisation loss of the MicroTCA data was critical and hardly recoverable. However, for the VME system, VME data appeared to be shifted with respect to the telescope data. This means that the VME content was recoverable using an offset algorithm that would eliminate this data conflict.
Figure 7.12 shows how the synchronisation loss acts on the VME data structure. While in the *No desynchronisation* case the telescope data and the VME data are matching within the same event number, the *Desynchronisation* case yields a shifted correspondence between event contents. Due to the synchronisation loss, the telescope data within event i is not anymore matching the VME data within the same event but rather matches the data within event $i + n_{offset}$, where n_{offset} is the introduced offset.

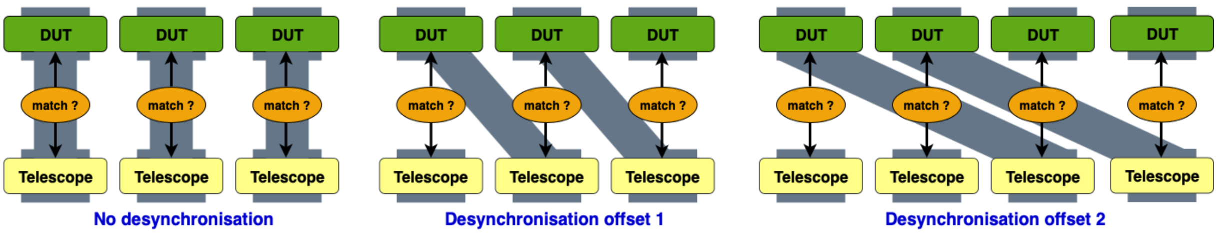

FIGURE 7.12 – Illustration to explain desynchronisation. The raw data originally belonging together are indicated by the grey background

In order to recover the synchronisation loss within the VME data, an offset algorithm was implemented. The algorithm is based on sensor efficiency calculation and uses the latter drops to detect synchronisation losses. It acts on bunches of 500 events and calculates the sensor efficiency. At the beginning of the run, the algorithm assumes a desynchronisation offset of $n_{offset} = 0$. As long as the sensor efficiency is found to be over an arbitrary threshold set to

20%, no synchronisation loss is registered. As soon as the sensor efficiency drops below 20%, as shown in Figure 7.11, a synchronisation loss is assumed and the desynchronisation offset is incremented for the next bunch of 500 events such as $n_{offset} = n_{offset} + 1$. The process is repeated all over the run in order to determine the offset associated to each bunch of 500 events. Figure 7.13 shows results of the offset algorithm applied to a run of 300k events.

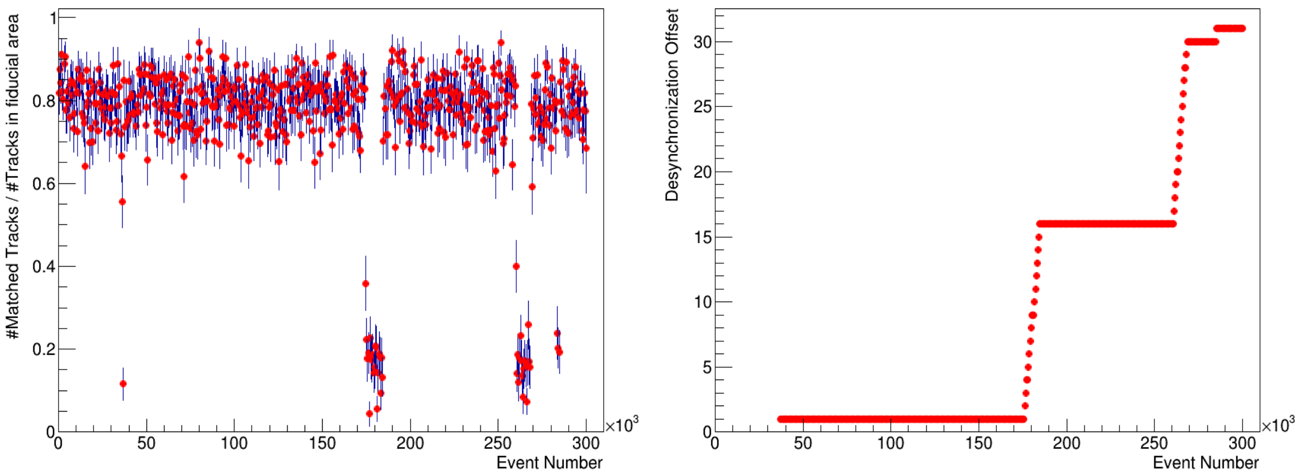

FIGURE 7.13 – Example of VME data synchronisation loss recovery (left) and the related offset values (right) using an offset algorithm

On the left plot, the efficiency drops, yielding a desynchronisation, call for an offset introduction shown on the right plot in order to recover the synchronisation loss.
In order for the analysis to be based on synchronised data, only the synchronised bunches were used. This means that only the flat sections of the offset plot were taken into consideration in the analysis. Moreover, since the MicroTCA synchronisation loss was hardly recoverable, only the VME data was used for the analysis.

7.5.2 Guard Ring Effects

As mentioned in Section 7.1, in order to ensure a unique correspondence between signal in the DUT and particle impact position, only events with one reconstructed track were selected. Moreover, to discriminate noise from signal pulses, a criteria was built assuming a noise of around 100Hz and a signal of 500MHz. As 100Hz/500MHz = 2.10^{-7}, this implies that 2.10^{-7}% of the noise is located over a $5.1\sigma_{Noise}$ cut. Therefore, the criteria used to discriminate signal pulses from noise was such as :

$$\frac{Signal\ Amplitude}{\sigma_{Noise}} > 5.1 \quad (7.4)$$

Only events with pulses fulfilling the signal cut criteria were used to map the particle tracks located within the diodes fiducial areas. Fiducial areas are shown in Figure 7.16. The latter were first determined by assuming a fiducial area larger than the sensor size, and the limits were then narrowed down to the metalisation pad excluding the guard ring for Sensor1, and to the metalisation pad including the guard ring for Sensor2. For the selected events, Figure 7.14 shows a distribution of the particle impact positions for Sensor1 (left) and Sensor2 (right) under a bias voltage of 300V.

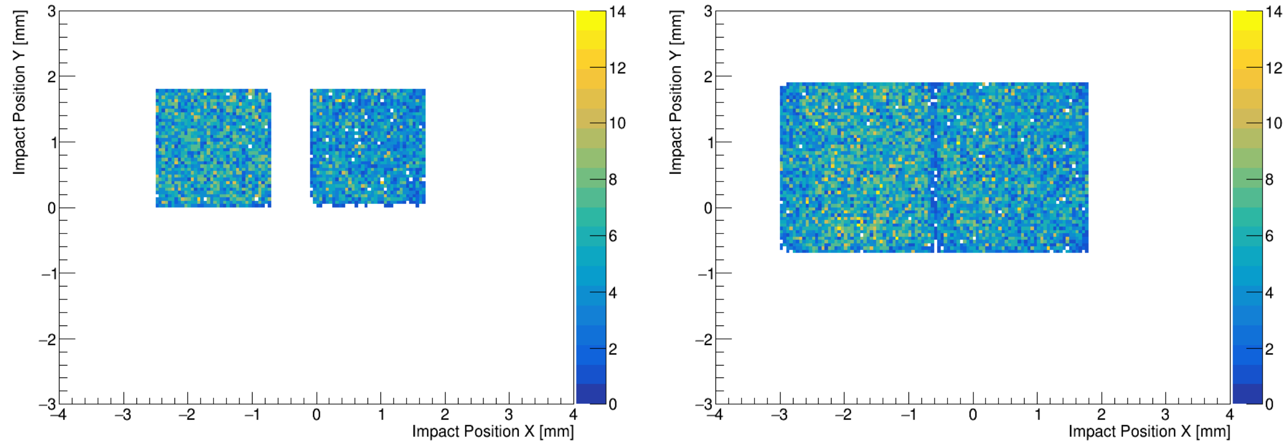

Figure 7.14 – Distribution of particle impact positions for Sensor1 (left) and Sensor2 (right) under a 300V bias voltage

For Sensor1 which has the grounded guard ring, the diodes size is observed to be of around $1.9 \times 1.8mm^2$, which is approximately the expected metalisation area. However, for Sensor2 which has a floating guard ring, the diodes size is observed to be of about $2.6 \times 2.8mm^2$, which is much larger than the metalisation area yielding an important overlapping area. The latter effect is mainly due to the fact that a floating guard ring strongly extends the sensor electrical field beyond the guard ring edges yielding a substantially larger sensor active area.

In order to investigate the position of the particles corresponding to the content of the shoulder appearing in amplitude spectra of Sensor2 as shown in Figure 7.7, amplitude spectra were built for the channels associated to Sensor2 using the signal cut criteria to eliminate the noise peak. Arbitrary cuts were then applied on the amplitude distribution in order to select only the particles associated to the shoulder content. Finally, the particle impact positions corresponding to signal below the cut were used to map the location of the latter.
Figure 7.15 shows Sensor2 amplitude spectra with the associated cuts (left) and the distribution of the particle impact positions associated to signals below the applied cut (right) for a run under 300V bias voltage.

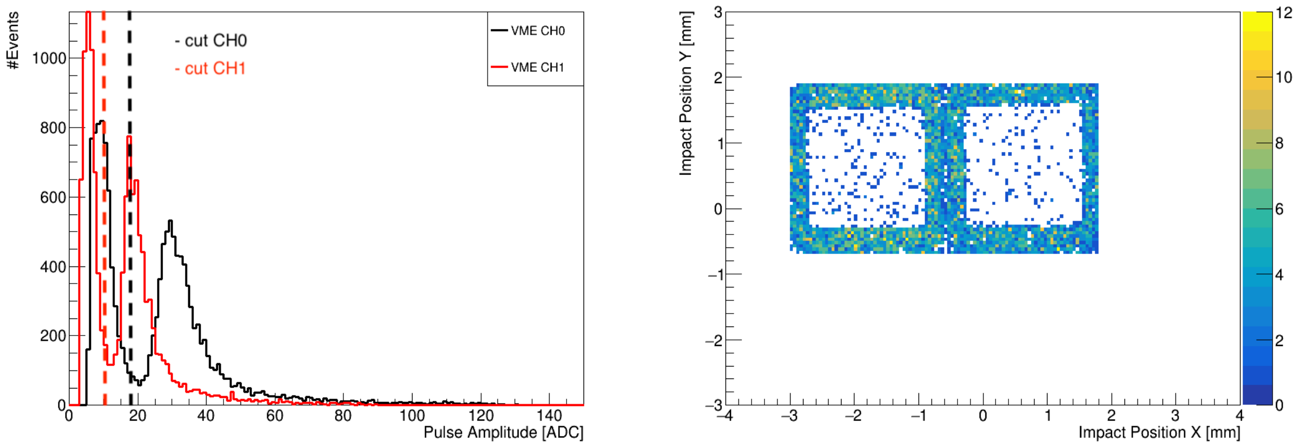

Figure 7.15 – Distribution of particle impact positions associated to the shoulder content of Sensor2 amplitude spectra at 300V bias voltage

The impact position mapping reveals that the content of the amplitude spectra shoulder is, as depicted in the hypothesis in Section 7.2, located around the guard ring. An extended explanation of this effect could be that in Sensor2 the bulk electrical field lines are strongly distorted on the edges due to the floating guard ring. In contrast to the parallel electrical field lines under the metalisation area, the bended lines on the edges yield a longer traveling time resulting in distorded signals and thus a reduced charge collection efficiency. This hypothesis could be further investigated using simulations and studies of the electrical field inside the sensor's volume.

7.5.3 Charge Collection Efficiency as a Function of Impact Position

When charged particles like an electron passes through the sensor, it creates electron-hole pairs that are separated by the applied electrical field within the sensor volume. The electrons then move to the positive electrode while the holes move to the negative one.
The Charge Collection Efficiency (CCE) is defined by using the charge measured as a signal on the electrodes when a particle crosses the sensor and reads as :

$$CCE = \frac{Q_{Signal}}{Q_{Expected}} \tag{7.5}$$

$$CCE[\%] = \frac{MPV[ADC] \cdot k[e/ADC]}{78[e/\mu m] \cdot d[\mu m]} \cdot 100 \tag{7.6}$$

where $Q_{Signal} = MPV[ADC] \cdot k[e/ADC]$ is the charge generated by the traversing particles and collected to produce a signal, and $Q_{Expected} = 78[e/\mu m] \cdot d[\mu m]$ is the expected generated and collected charge that depends on the sensor thickness.

The CCE as a function of the beam particle impact position was studied at a bias voltage of 300V for both Sensor1 and Sensor2. The homogeneity of the signal response is then obtained, and edge effects as well as guard ring effects become visible.
In order to perform the analysis, fiducial areas slightly larger than the metalisation pad area are defined. For Sensor1, the fiducial areas don't include guard rings and are restricted to metalisation pad areas. For Sensor2, the fiducial areas include both the metalisation pad areas and the guard rings and the CCE measurement is done for each of them separately to allow comparision.
Each fiducial area was divided into $50\mu m$ width strips along the x-axis in order to measure the CCE as a function of the x-position. Figure 7.16 shows the defined fiducial areas for both Sensor1 and Sensor2 diodes.

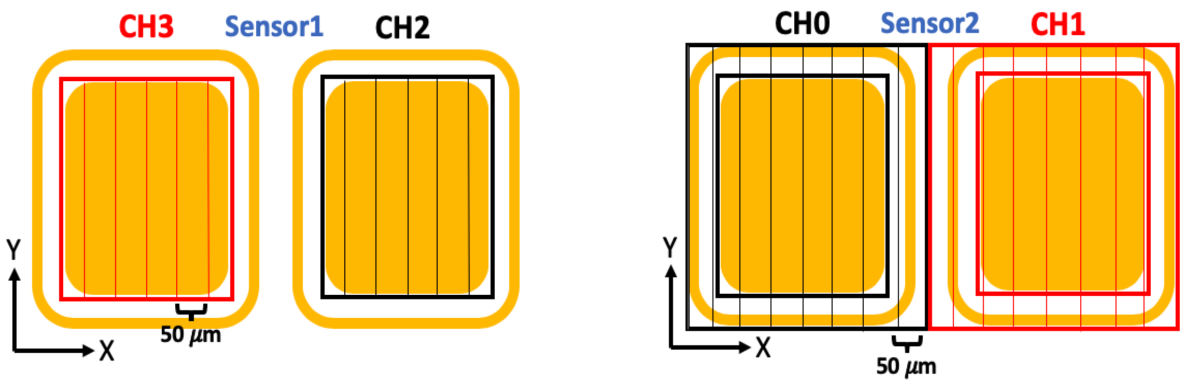

FIGURE 7.16 – Fiducial areas defined for both Sensor1 diodes (left) and Sensor2 diodes (right)

Figure 7.17 shows results of CCE measurements as a function of the x-position for Sensor1 and Sensor2 at a bias voltage of 300V. To achieve higher statistics, 2 adjacent strips were merged and CCE value was extracted using all the particle content of their x-position. As in Sensor2 CH0 is a non-calibrated channel, it was excluded from the measurement.
Sensor1 that has the guard ring grounded shows a constant CCE of 95% over the diodes range. For Sensor2 in which the guard ring was kept floating, CCE in the central position appears to be around 87%. This low value is most likely due to the imperfect calibration of Sensor2 channels. On the guard ring the CCE is observed to drop to around 25%. The latter drop is most likely due to a strongly affected electrical field inside the sensor volume in the area of the floating guard ring. But again, this hypothesis could be verified by simulations and studies of how the electrical field distribution inside the sensor volume is affected by the floating guard ring.

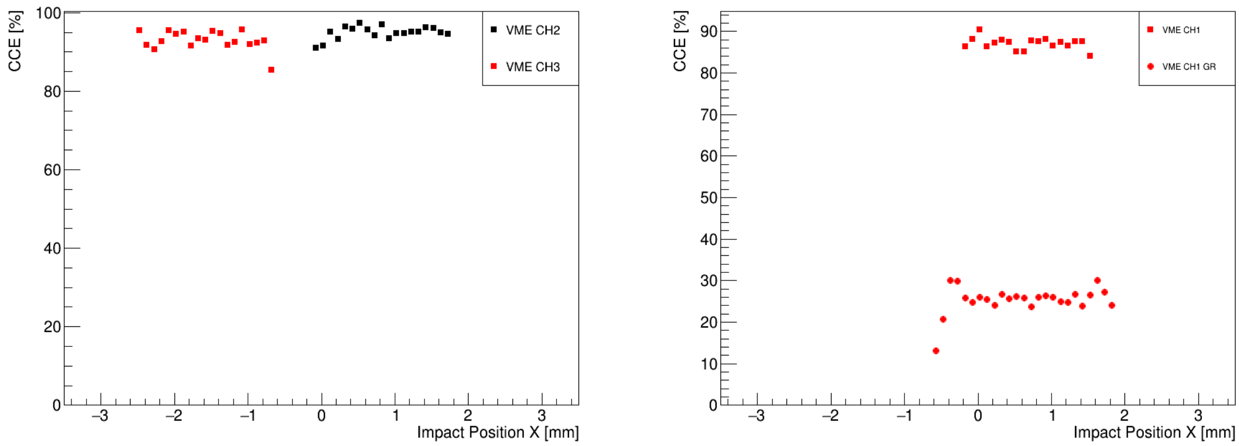

FIGURE 7.17 – CCE measurements as a function of sensor x-position for Sensor1 (left) and Sensor2 (right) at 300V bias voltage

8 Conclusion

As part of the CMS detector LS2 upgrades, the BCM1F sub-detector was redesigned to meet higher operation performance for the coming Run3. A new version of the detector based on AC-coupled double diode Silicon sensor was produced and provided for tests. For that purpose a test-beam campaign was held by the BCM1F group at the DESY test-beam facility using the DESYII beam and the EUDET beam telescope. The EUDAQ framework, in which the BCM1F DAQ systems were integrated, was used for data acquisition. BCM1F related EUDAQ Producers and Converter-Plugins were implemented, allowing for a controled configuration and synchronous running of both the VME and MicroTCA systems with respect to the other test beam devices. Additionaly, the native EUDAQ Online Monitor was extended in order to include specific plots related to the BCM1F DAQ systems and provide a fast quality check of the recorded data. The aim of the testbeam campaign was to record enough data in order to study the performance of AC-coupled silicon sensors mounted on the BCM1F test board.

A big effort was and is still invested in solving synchronisation loss issues that were discovered after the test-beam data taking. They appear to be critical for the MicroTCA data while still recoverable for the VME data. An attempt to recover synchronisation of the VME system data was undertaken and was proven to be successful to a certain extent.
The preliminary results using the recovered data presented in the scope of this thesis are very promising for the new version of the detector as they yield a good signal to noise separation in the amplitude spectrum, and an almost 100% effective sensor thickness for diodes with the grounded guard ring. Moreover, it has been demonstrated that a floating sensor guard ring introduces some edge effects that appear for example as a shoulder in the signal-noise separation region in the amplitude spectra, or as charge collection efficiency drops in the edge area, highly affecting the signal-noise discrimination that is essential for luminosity measurements. The latter effect was explained by the electrical field extension introduced by a floating guard ring around the metalisation pad. However, additional work needs to be done in order to improve different aspects of the various analyses, namely the track reconstruction and the detector calibration. In fact, on the one hand the track reconstruction should ideally include a reconstruction algorithm that takes into consideration multiple scattering effects. On the other hand, calibration constants should be re-evaluated for one of the sensors in order to provide a more consistent comparision basis of the two sensors. The final objective is then to understand better the various sensor features in order to improve the design and the production of the C-shaped modules and the AC-coupled silicon sensors for the Run3 of the LHC starting in 2021.

References

[1] CERN FAQ - LHC the guide . http ://cdsweb.cern.ch/record/1165534/files/, 2009.

[2] A. Seiden. Characteristics of the ATLAS and CMS detectors. *Phil. Trans. R. Soc. A (2012) 370, 892–906*, 2012.

[3] The CMS Collaboration. Observation of a new boson at a mass of 125 GeV with the CMS experiment at the LHC. *Physics Letters B 716 (2012) 30–61*, 2012.

[4] S. de Capua and al. Luminosity Measurements at LHC. *Il Nuovo Cimento, Vol. B123*, 2008.

[5] Olena Karacheban. *Luminosity Measurement at CMS*. PhD thesis, Brandenburg University of Technology Cottbus-Senftenberg, 2016.

[6] S.Van-Der-Meer. LCalibration of the Effective Beam Height in the ISR. *CERN-ISR-PO-68-31*, 1968.

[7] T. Sakuma and T. McCauley. Detector and Event Visualization with SketchUp at the CMS Experiment. *J. Phys. : Conf. Ser. 513 022032*.

[8] Frank Hartmann. Evolution Of Silicon Sensor Technology In Particle Physics. *Springer tracts in modern physics. Springer, Berlin*, 2009.

[9] Georg Auzinger. *Silicon Sensor Development for the CMS Tracker Upgrade*. PhD thesis, Vienna University of Technology, 2013.

[10] M. Tanabashi and al (Particle Data Group). Review of Particle Physics. *Phys. Rev. D 98, 030001*, 2018.

[11] L. Landau. On the energy loss of fast particles by ionization. *J.Phys.(USSR) 8*, 1944.

[12] C. Grupen and B. Shwartz. Particle Detectors. *Cambridge University Press*, 2008.

[13] Jan Kaplon Dominik Przyborowski and Piotr Rymaszewski. Design and Performance of the BCM1F Front End ASIC for the Beam Condition Monitoring System at the CMS Experiment. *IEEE Transactions on Nuclear Science, Vol. 63, NO. 4*, Aug 2016.

[14] *CMS Tracker Optical Readout Link Specification.*

[15] *Linear Laser-Driver IC.*

[16] Alexander Jonas Rude. New Peak Finding Algorithm for the BCM1F Detector of the CMS Experiment at CERN. Master's thesis, Erns-Abbe-Hochschule Jena University of Applied Sciences, 2018.

[17] VME MOD V1721-V1731 Technical Information Manual, Manual Rev 22. Technical report, CAEN, 2013.

[18] A.A.Zagozdzinska. The CMS Fast Beams Condition Monitor Backend Electronics based on MicroTCA technology. Technical report, CMS CR -2015/315, 2015.

[19] H. Jansen & al. Performance of the EUDET-type beam telescopes. *ArXiv :1603.09669*, 2016.

[20] D. Cussans. Description of the JRA1 Trigger Logic Unit (TLU), v0.2c. Technical report, EUDET project, 2009.

[21] I.Rubinskiy. An EUDET/AIDA pixel beam telescope for detector development. *Physics Procedia 37* , 2012.

[22] *EUDAQ User Manual.*

[23] *CAEN Digitizer Library, Library of functions for CAEN Digitizer high level management, 2018.*

[24] *GLIB v3 User Manual.*

[25] D. Eckstein. Semiconductor Detectors. *Solid State Detectors Lectures - DESY*, 2012.